Remote Sensing of Environment 312 (2024) 114315

Contents lists available at ScienceDirect

Remote Sensing of Environment

journal homepage: www.elsevier.com/locate/rse

First lunar-light mapping of nighttime dust season oceanic aerosol optical depth over North Atlantic from space

Meng Zhou [a,b,c,*], Jun Wang [a,b,d,*], Xi Chen [b,d], Yi Wang [d,e], Peter R. Colarco [f], Robert C. Levy [g], Steven D. Miller [h]

[a] Interdisciplinary Graduate Program in Geo-Informatics, The University of Iowa, Iowa City, IA 52242, USA
[b] Center for Global and Regional Environmental Research, and Iowa Technology Institute, The University of Iowa, Iowa City, IA 52242, USA
[c] Now at: Goddard Earth Sciences Technology and Research (GESTAR) II, University of Maryland – Baltimore County, Baltimore, MD 21228, USA
[d] Department of Chemical and Biochemical Engineering, The University of Iowa, Iowa City, IA 52242, USA
[e] Now at: Hubei Key Laboratory of Regional Ecology and Environmental Change, School of Geography and Information Engineering, China University of Geosciences, Wuhan 430074, China
[f] Atmospheric Chemistry and Dynamics Laboratory, NASA Goddard Space Flight Center, Greenbelt, MD 20771, USA
[g] Climate and Radiation Laboratory, NASA Goddard Space Flight Center, Greenbelt, MD 20771, USA
[h] Cooperative Institute for Research in the Atmosphere, Colorado State University, Fort Collins, CO 80523, USA

ARTICLE INFO

Editor: Dr. Menghua Wang

Keywords:
Nighttime aerosol optical depth
Visible band AOD
Oceanic AOD
Sahara dust plume
Dust transport
Algorithm development
VIIRS
DNB
Reflected moonlight
Passive remote sensing over ocean

ABSTRACT

This paper presents the Nighttime Ocean Aerosol Optical Depth (AOD) Retrieval Algorithm (NOARA), an innovative method for deriving the oceanic AOD from the reflected moonlight observation of Day-Night Band (DNB) aboard the Visible Infrared Imaging Radiometer Suite (VIIRS) over ocean surfaces. Building upon the recent development of nighttime AOD retrievals for rural/wild areas over land, the NOARA introduces several advancements tailored for oceanic application: (a) the new dust and sea salt optical property models based on the AERONET observation; (b) the Cox-Munk bidirectional reflectance distribution function (BRDF) model that better represents the ocean surface reflectance; (c) the new internal cloud and dust masking schemes for the ocean areas. Case studies show that the nighttime AODs are in good consistency with multiple AOD measurements such as from AERONET and CALIOP. The algorithm fills the observational gap for a comprehensive understanding of the diurnal cycle of the dust transport over the ocean and has the potential to provide vital information to better constrain the chemical transport model.

1. Introduction

Atmospheric aerosols have garnered significant attention from the scientific community in recent decades due to their complex and wide-ranging impacts on the environment, weather, climate, air quality, and public health. Fine-size particles with diameters smaller than 2.5 μm, also known as $PM_{2.5}$, are associated with a staggering number of deaths globally, with estimates as high as 9 million annually (Pye et al., 2021). Furthermore, aerosol-cloud interactions contribute significantly to the largest sources of uncertainty in understanding the Earth's changing energy budget (Pörtner et al., 2022), making them relevant to climate and climate change. Aerosols play a role in the geobiological cycle as well; For example, the deposition of iron-rich nutrients from terrigenous matter lofted into the atmosphere can enhance biological productivity both in forests and in the ocean (Richon et al., 2018; Rizzolo et al., 2017; Westberry et al., 2023). Accurately quantifying the role of aerosols in Earth systems requires comprehensive characterization of their distribution globally with full spatial and temporal coverage.

Over the past two decades, satellite measurements have become increasingly prevalent as a tool for mapping the global distribution of atmospheric aerosol loading. Satellite-based aerosol monitoring offers insights into the smoke and dust events by detecting their presence (Singh et al., 2019), distinguishing their species, and retrieving their optical properties such as aerosol optical depth (AOD)(Hsu et al., 2019; Lyapustin et al., 2011; Sawyer et al., 2020; Sayer et al., 2018; Wang et al., 2021), fractions of either fine mode AOD or non-spherical AOD (Kahn et al., 2009), and the aerosol optical centroid height (Chen et al., 2021; Lu et al., 2023; Pierangelo et al., 2004; Vandenbussche et al.,

* Corresponding authors at: Interdisciplinary Graduate Program in Geo-Informatics, The University of Iowa, Iowa City, IA 52242, USA.
E-mail addresses: meng-zhou-1@uiowa.edu (M. Zhou), jun-wang-1@uiowa.edu (J. Wang).

https://doi.org/10.1016/j.rse.2024.114315
Received 26 June 2023; Received in revised form 14 June 2024; Accepted 9 July 2024
Available online 27 July 2024

2013; Xu et al., 2017). Beyond traditional physics-based retrieval algorithms in the daytime, there are efforts to leverage state-of-the-art data-driven techniques to develop artificial intelligence (AI) models for aerosol retrieval (Yuan et al., 2020). One approach involves training models on the forward radiative transfer process to replace the physics-based radiative transfer simulation or lookup table (Fan et al., 2019; Chen et al., 2022; Gao et al., 2023; Tao et al., 2023). The advantages of this approach include the extensive amount of simulations, which provide the AI model with a robust capacity for aerosol classification, and a significantly faster operational speed compared to physics-based radiative transfer simulations. However, it is subject to noise and observational uncertainties when applied to real retrieval since the training set is purely simulated. Additionally, efforts have been made to train machine learning models for AOD estimation directly from collocated satellite observations and AOD measurements (Bao et al., 2023; Di Noia et al., 2017; Niang et al., 2006), addressing the observational uncertainties faced by previous AI training strategies. Nonetheless, the applicability of these models is limited to specific instruments and observational conditions. Furthermore, post bias correction (Lanzaco et al., 2017; Lary et al., 2009) methods are also developed to improve the AOD retrieval accuracy. However, their effectiveness heavily relies on the accuracy of upstream AOD retrievals. Apart from narrow-swath lidar observations like those from Cloud-Aerosol Lidar with Orthogonal Polarization (CALIOP; Jiang et al., 2024; Winker and Hunt, 2007; Winker et al., 2009) and Cloud-Aerosol Transport System (CATS; McGill et al., 2015), the majority of the space-borne sensors measuring aerosols provide only daytime aerosol information. This limitation stems from their reliance on radiance (and polarization) measurements in the solar spectrum. This leads to a large unknown on the movement and spatial distribution of aerosols at nighttime.

To fully understand the daily (24-h) variation of the atmospheric aerosols, a minimum sampling interval of 12 h is required, as per the Nyquist-Shannon sampling theorem (Oppenheim et al., 1997). This observational interval has also been proven to be critical for improving the accuracy of model forecast ability in data assimilation systems (Lee et al., 2017). To meet that requirement, numerous endeavors have been put forth to retrieve nighttime AOD through the utilization of passive remote sensing observations, specifically the Visible Infrared Imaging Radiometer Suite (VIIRS; Miller et al., 2013; Schueler et al., 2002), which carries a Day/Night Band (DNB) sensor for observing the Earth at night in the visible/near-infrared part of the spectrum. Zhou et al. (2021) were the first to design an algorithm to retrieve the nighttime AOD from the reflected moonlight measured by the VIIRS DNB in the rural/wild area, where DNB observations are less affected by the city lights. Case studies demonstrated the feasibility of using reflected moonlight to retrieve AOD at night and the value of nighttime AOD for better understanding the nonlinearity of the regional smoke transport over time.

To date, mapping of nighttime AOD over the ocean surface from reflected moonlight has not been attempted. In this work, we revise the nighttime AOD retrieval technique developed by Zhou et al. (2021) over rural land to develop the Nighttime Ocean AOD Retrieval Algorithm (NOARA) for the tropical Atlantic Ocean surface during the dust season. While several researches have investigated the possibilities of the retrieval information of the dust through thermal infrared channels (De Paepe and Dewitte, 2009; Klüser et al., 2011; Zheng et al., 2022; Zheng et al., 2023), this research represents the first attempt to retrieve *visible* band AOD of dust particles over the ocean at night. The importance of this work lies in the fact that dust plumes can drift with the atmospheric wind up to 100 km per hour, and dust AOD values can exhibit large daily variations (STD/mean on the daily basis can be up to 50% or larger) over the ocean (Christopher et al., 2003; Wang et al., 2003; Wang et al., 2004). As such, any information on mapping dust AOD at night over the ocean can contribute to the much-needed characterization and prediction of dust plume movement for air quality and visibility applications. We test our algorithm for the Trans-Atlantic dust aerosols in summer over the ocean.

We organize this paper as follows: In Section 2, a brief introduction is given for VIIRS DNB sensor and the retrieval and validation datasets used in NOARA. Details of the NOARA scheme are described in Section 3. Retrieval results assessment with CALIOP data, AErosol RObotic NETwork (AERONET) lunar AOD, Moderate Resolution Imaging Spectroradiometer (MODIS) and VIIRS daytime AOD, and the The Infrared Atmospheric Sounding Interferometer (IASI) IR AOD are given in Section 4, together with a comparison with re-analysis of AOD from The Modern-Era Retrospective analysis for Research and Applications, Version 2 (MERRA-2). Section 5 summarizes the paper.

2. Senor, data, and numerical model

The NOARA framework is devised to leverage the viable reflected moonlight observations from the VIIRS DNB (Section 2.1) to oceanic AOD retreival. This process is facilitated through a look-up table (LUT) approach, underpinned by a state-of-the-art radiative transfer code (Section 2.3). CALIOP AOD (532 nm), IASI AOD (10 μm), AERONET lunar AOD (550 nm), and other datasets (such as meteorological fields and AOD field of MERRA-2, as in Section 2.2) are used to evaluate the retrieval (Section 2.2).

2.1. VIIRS nighttime observation

The VIIRS sensor is a crucial component of the Joint Polar Satellite System (JPSS) series of polar-orbiting operational environmental satellites of the United States. The first VIIRS sensor was launched in 2011 onboard the Suomi-NPP (S-NPP) satellite. The Local Time of Ascending Node (LTAN) of S-NPP satellite is 1330 and the corresponding descending node, which enables the nighttime Earth observation, is approximately 0130 local time. The second VIIRS sensor is carried on the NOAA-20 satellite and shares the same orbit plane as S-NPP but is half-orbit (50 min) ahead. The third VIIRS sensor was launched in November 2022 as part of the payload of the NOAA-21 satellite, sharing the same orbit plane as S-NPP and NOAA-20 satellites. Currently, NOAA-21 is positioned between the S-NPP and NOAA-20 satellites, with approximately a 25-min time difference. Specifically, NOAA-21 is approximately 25 min ahead of S-NPP and 25 min behind NOAA-20. Once NOAA-21 is officially declared as the primary VIIRS sensor for the 1330 LTAN, NOAA-20 will be shifted 25 min ahead to ensure the required half-orbit separation between NOAA-20 and NOAA-21.

VIIRS images the Earth through 3 spatial resolutions. It comprises five imagery bands, known as I-bands, which observe the Earth in an approximate spatial resolution of 375 m. There are also sixteen moderate-resolution bands (M-bands) that provde image of the Earth at 750-m resolution. Uniquely, VIIRS also features a panchromatic Day/Night Band (DNB), a specialized low light sensor, that operates at a nominal spatial resolution of 742 m. VIIRS DNB covers wavelengths from approximately 500 nm to 900 nm and is designed with three gain stages, it accommodates a dynamic range of seven orders (from 3×10^{-9} to 0.02 W cm^{-2} sr^{-1}) in DNB, enabling the detection of low light such as the upwelling artificial city light (Wang et al., 2016; Elvidge et al., 2017; Li et al., 2019; Min et al., 2020; Min et al., 2021), pyrogenetic light (Elvidge et al., 2013; Polivka et al., 2016; Wang et al., 2020a; Zhou et al., 2023), and the reflected lunar radiances (Zhou et al., 2021) for application across a wide range of topic including surface air quality (Fu et al., 2018; Wang et al., 2016), nighttime aerosol parameterization (Johnson et al., 2013; McHardy et al., 2015; Zhou et al., 2021), nighttime cloud retrieval (Walther et al., 2013), nigtthime fire characterization (Wang et al., 2020a; Zhou et al., 2023), urbanization (Song et al., 2021), environmental justice (Wang et al., 2020b), public health (Xiao et al., 2023a; Xiao et al., 2023b), et al. For more detailed information and applications of the VIIRS DNB, please refer to the provided references.

2.2. Data for retrieval and algorithm validation

The primary dataset used for retrieval of oceanic AOD is the full set of S-NPP VIIRS Level-1 B data, including the calibrated radiance products of I-band (VNP02IMG), M-Band (VNP02MOD), and DNB (VNP02DNB). Other VIIRS datasets used include the geolocation products for the corresponding three spatial resolutions (VNP03IMG for I-band, VNP02MOD for M-band, and VNP03DNB for DNB). All the VIIRS datasets can be accessed through the NASA Level-1 and Atmosphere Archive & Distribution System (LAADS, https://ladsweb.modaps.eosdis.nasa.gov/). Since this is the first demonstration of using VIIRS DNB to retrieve AOD over ocean surface, we applied the most rigorous quality control to all the Level-1 B datasets. Only pixels with quality flags smaller than 1 (e.g., highest quality) are considered in the retrieval work. For additional datasets used as inputs for the NOARA include:

- We utilized the assimilated meteorological (M2T3NVASM) and aerosol (M2T3NVASM) fields from the MERRA-2 (Buchard et al., 2017; Gelaro et al., 2017; Randles et al., 2017). The 2-m wind speed fields, part of the M2T3NVASM, provide the input for the Cox-Munk model (Cox and Munk, 1954), was used to account for the wind-triggered bidirectional reflectance distribution function (BRDF) effects on the ocean surface. The surface temperature field, also part of the M2T3NVASM, was used as ancillary information for the internal cloud masking (Section 3.3) of the NOARA. M2T3NVASM is reported every 3 h. For a granule of VIIRS observations, we first applied linear interpolation to map those two fields to the time that S-NPP satellite overpass and then used bi-linear interpolation to obtain those physical parameters of interest at the VIIRS footprints.
- We utilized the Global Ozone Monitoring Experiment-2 (GOME-2) surface Lambert-equivalent reflectivity (LER) database (Tilstra et al., 2017) to account for the Lambertian surface reflectance component of the ocean surface. Similar to the MERRA-2 surface temperature field, bi-linear interpolation was used to interpolate the gridded GOME-2 LER to the DNB footprint. It is worth noting that we neglected the spectral dependence of the LER and only use band 11 (757.6 nm) LER to represent the surface reflectance, in order to reduce computational complexity, as the surface reflectance over water exhibits less variation (<1.5% with respected to 757.6 nm reflectance) across the DNB spectrum range (Tilstra et al., 2017).

The following datasets are utilized in order to validate the NOARA AOD in terms of individual point, spatial distribution, and overall magnitude, respectively:

- Nighttime ground AOD measurements from AERONET LUNAR AOD Version 3 (V3, τ_{LNR}) PROVISIONAL (https://aeronet.gsfc.nasa.gov/cgi-bin/draw_map_display_aod_v3_lunar) were used to evaluate the DNB retrievals. As stated in Zhou et al. (2021), the current V3 lunar AOD is considered provisional due to the ongoing development of the AERONET retrieval algorithm and uncertainty in the calibration (Giles et al., 2019). We used the same approach as illustrated in Zhou et al. (2021) to collocate the AERONET AOD with DNB AOD. Specifically, we first interpolated the AERONET AOD to 550 nm using the associated Angstrom Exponent available in the V3 data. Then, a one-hour temporal window was applied to acquire the 550 nm AODs over the VIIRS overpass time to from the temporal mean of the AERONET AOD and corresponding standard deviation for comparison. We required that within the one-hour time window at least two AERONET samples should be valid. Equivalently, a 50 km diameter circle centered at the AERONET site was used to acquire DNB retrievals to form the collocated DNB AOD counterparts.
- The level 2 (Version 4.10) CALIOP nighttime aerosol profile (Getzewich et al., 2016; Tackett et al., 2018) was used to validate the NOARA in the senses of the AOD retrieval accuracy and the spatial gradient. The CALIOP nighttime column AOD (τ_{CN}) at 532 nm was obtained by integrating the aerosol extinction coefficient along the altitude vertically at its native horizontal resolution of 5 km. Considering the roughly one to two hours overpass difference between CALIOP and VIIRS DNB, τ_{CN} was aggregated to 50 km (Martins et al., 2017).
- The daytime VIIRS Dark Target (AERDB_L2_VIIRS_SNPP, DT; Sawyer et al., 2020), Deep Blue (AERDT_L2_VIIRS_SNPP, DB; Sayer et al., 2018) AOD, MODIS DT AOD (3 km resolution, MOD04 and MYD04; Remer et al., 2005) were compared with the NOARA AOD. VIIRS DT & DB and MODIS DT AOD are only valid during the daytime and serve as references for spatial distribution and the overall magnitude of the AOD retrieval.
- The IASI Nighttime Level 2 dust AOD retrieval (τ_{IA}, Vandenbussche et al., 2013) was also employed in this study as a reference (not ground truth) to cross-check the retrieval performance. These three IASI sensors, onboard the METOP A, B, and C satellites, retrieve the lofting dust optical depth and the dust layer height using the thermal infrared observations. By design, IASI sensors have spatial resolution of 12 × 12 km at nadir (39 × 20 km at the edge of the swath) and twice per day overpasses at nominal 9:00 a.m. and 9:00 p.m. LST, providing glimpses of the dust optical depth on the infrared channels. Unlike MODIS and VIIRS which report their AOD products at 550 nm as grided data, the IASI level 2 dust AOD, delivered by the atmosphere Data and Service Center of European (AERIS, https://iasi.aeris-data.fr/dust-aod_iasi_a_arch/), is reported at 10 μm in the Geo-Trajectory format. To compare the DNB AOD with IASI IR AOD quantitatively, the IASI AODs were first resampled to MERRA-2's 0.5° × 0.625° climate modeling grids (CMG). The METOP A-C IASI IR AODs are then combined into a single image for improved spatial coverage, as the overpass times of the three IASI sensors are very close. It should be noted that while several research studies have demonstrated the feasibility of IASI retrieval (Callewaert et al., 2019; Capelle et al., 2014; Clarisse et al., 2019; Peyridieu et al., 2013; Zheng et al., 2022), in this research, IASI data was used solely to evaluate and cross-validate the spatial distribution agreement between the difference retrievals.
- The MERRA-2 AOD analysis (M2I3NXGAS) data was also utilized as an example to illustrate the model's projected evolution of oceanic aerosols and serves as a baseline for evaluating the incremental benefits of the NOARA AOD.

2.3. Nighttime UNL-VRTM

We employed the UNified Linearized Vector Radiative Transfer Model (UNL-VRTM; Wang et al., 2014) for radiative transfer simulation, generating the essential look-up table for the oceanic aerosol retrieval in this research. The model's latest developments are detailed in Wang et al. (2020c). Pertinent to this study, a lunar irradiance database developed by Miller and Turner (2009) was integrated for simulating the reflected moonlight. This database spans from 202 nm to 2800 nm, with a spectral resolution of 1 nm and a moon phase resolution of 1°, thoroughly encompassing the spectral bandpass of VIIRS DNB. Additionally, an astrophysical code was incorporated to compute the celestial geometry of the Sun-Earth-Moon system (Schlyter, 2010). This aids in determining the sensor's geometrical configuration for moonlight observation, including zenith and azimuth, moon phase angle, etc. These innovative enhancements empower the UNL-VRTM to accurately simulate the moon-phased based backscattered radiation fields illuminated the Moon, within an uncertainty of ±10% (Wang et al., 2020c). The UNL-VRTM utilizes the linearized Mie and T-matrix codes to determine optical properties such as single scattering albedo (SSA) and phase function, based on aerosol microphysics, e.g. particle size, shape, refractive index, etc. This was used for simulating the maritime aerosols model for the relative clean atmosphere condition and the fine mode component of the dust aerosol model (Section 3.1). The model also allows customization of SSA and phase function, aiding in characterizing

the non-spherical properties of dust aerosols (Section 3.1).

3. Nighttime Ocean AOD retrieval algorithm

Fig. 1 is the flowchart of the NOARA algorithm. The NOARA is a single channel, LUT-based retrieval algorithm. It relies on additional assumptions on the aerosol model (Section 3.1) and surface reflectance. It essentially takes four steps to retrieve the nighttime ocean AOD:

1) Calculate the DNB reflectance at the top of atmosphere (TOA), leveraging DNB radiance and Sun-Earth-Moon geometry information provided in the Level-1B data (Section 3.2)
2) Mask out area affected by cloud and moon glint (Section 3.3)
3) Invert AOD from DNB reflectance in the cloud-free, dust-free and moon glint-free pixels by using a pre-calculated maritime LUT (Section 3.1)
4) Revise inversion of Step 3 for any pixels that is flagged as dust or whose AOD value exceeds 0.25, this time using a dust aerosol LUT (Section 3.1)

We describe each of the steps in detail in the following subsection. It should be noted that due to the signal-to-noise ratio (SNR) limitations of the VIIRS nighttime reflected moonlight observations, NOARA will only retrieve nighttime AOD when the Moon Illumination Fraction (MIF) is >75%—spanning from Waning Gibbous to Full Moon, and then to Waxing Gibbous. This confines NOARA's retrieval capability to approximately 7 to 10 days per lunar cycle (~28 days), depending on the location. This threshold aligns with the land AOD retrieval algorithm that uses the VIIRS nighttime moonlight observations, and it is slightly higher than the 50% threshold used by AERONET, which spans from the third quarter to the full moon, and then to the first quarter, as AERONET monitors the direct moonlight.

3.1. Aerosol model and radiative transfer simulation

Accurate parameterization of the aerosol optical properties is vital for achieving credible results with a single-channel retrieval algorithm. For the experimental domain under consideration, we employed two aerosol models (Tables 1 and 2) to represent the potential oceanic aerosol: the dust (Table 1) and the background maritime (Table 2) models, with the latter adopted from Sayer et al. (2018). The maritime aerosol model was derived on the assumption of a relative clean atmosphere, leading to an AOD upper limit of 0.25, as detailed in Sayer et al. (2018). This upper boundary was utilized in NOARA to determine the need for AOD revision, as illustrated in the Step 4. We made a simple assumption that for observations whose initial AOD retrievals were >0.25, dust contributed to the rise of the TOA reflectance. Consequently, a revision of retrieval by using the dust LUT was performed. It is important to recognize that, as a single-channel retrieval algorithm, the use of multiple aerosol models necessitates assumptions that are independent of the observations. This limitation of NOARA is acknowledged and highlights the need for further investigation. Future research is anticipated to synthesize more prior information, thereby improving aerosol model segregation and enhancing the overall effectiveness of the algorithm.

Table 1
Aerosol model - dust.

Parameter Name	Short Name	Value
Volume Median Radius (Fine Mode)	VMR-F	0.19
Effective variance (Fine Mode)	V_{eff}-F	0.44
Fine mode fraction	FMF	$-0.0232 \ln \tau + 0.22747$
Refractive index (440 nm, 675 nm, 870, 1020)	$M_r + M_i$	$1.43 + 0.001i$
Dust SSA (440 nm)	SSA_{440}	$-0.0018 \ln \tau + 0.912$
Dust SSA (675 nm)	SSA_{675}	$0.005 \ln \tau + 0.984$
Dust SSA (870 nm)	SSA_{870}	$0.009 \ln \tau + 0.987$
Dust SSA (1020 nm)	SSA_{1020}	$0.01 \ln \tau + 0.988$
AOD at 550 nm	N_τ	0.25, 0.30, 0.40, 0.60, 0.80, 1.00, 1.20, 1.40, 1.60, 1.80, 2.00, 2.50, 3.00, 4.00, 5.00

The dust aerosol model is represented as a bi-modal distribution with a coarse mode for dust and a fine mode for background aerosol with fine mode fraction (FMF) dynamically changed with AOD. Their optical properties and microphysics parameters were derived from AERONET Version 3 aerosol optical depth and inversion products at Cape Verde since 1994 for both modes. To differentiate dust within the AERONET data, we filtered the AERONET V3 data using criteria of a FMF at 500 nm

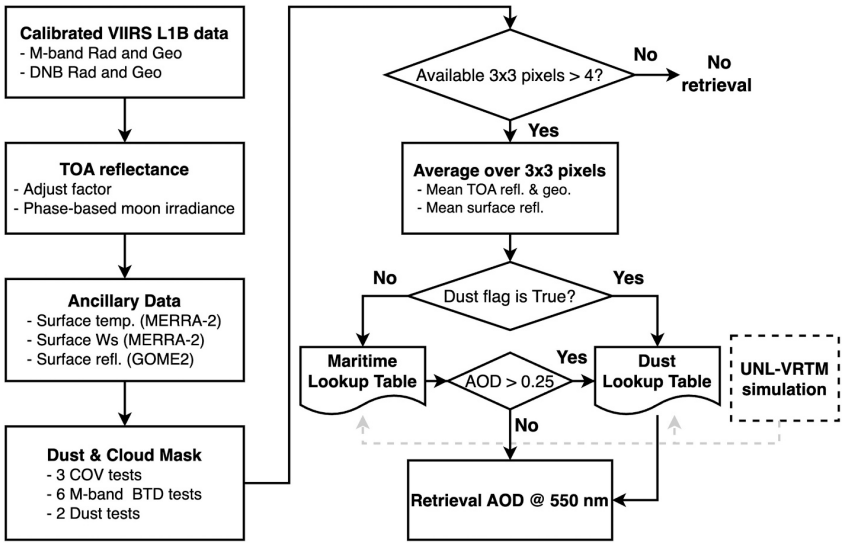

Fig. 1. Flowchart to the Nighttime Ocean AOD Retrieval Algorithm (NOARA).

Table 2
Aerosol model – maritime aerosol.

Parameter							
Total AOD	0.001	0.04	0.08	0.12	0.16	0.2	0.25
Fine mode fraction	0.1	0.2	0.3	0.4	0.5	0.7	0.8
Coarse mode AOD	0.0009	0.032	0.056	0.072	0.08	0.06	0.05
Fine mode AOD	0.0001	0.008	0.024	0.048	0.08	0.14	0.2
Coase mode volume concentration (um3/um2)	9.653e-04	3.432e-02	6.006e-02	7.722e-02	8.580e-02	6.435e-02	5.363e-02
Find mode volume concentration (um3/um2)	2.279e-05	1.823e-03	5.469e-03	1.094e-02	1.823e-02	3.191e-02	4.558e-02

smaller than 0.2 and a coarse mode AOD >0.25 (Sayer et al., 2018). To prepare the necessary inputs, e.g. SSA, AOD, and phase function, for radiative transfer simulation of the coarse model aerosol, which is primarily dominated by the non-spherical dust, we followed the approach outlined by Zhou et al. (2021) and Xu and Wang (2015) to apply a cluster analysis on the selected AERONET dust-dominated inversion. We modeled the SSA of the coarse mode aerosol as a function of the AOD and wavelength (Fig. S2). Specifically, a logarithmic regression technique was employed to establish the AOD dependence of the coarse mode SSA at four specific wavelengths: 440, 675, 870, and 1020 nm, with respect to the AOD at 675 nm. Subsequently, for each of the sub-wavelengths within DNB, a two-dimensional cubic interpolation was applied to obtain the wavelength dependent SSA for a given AOD at 675 nm. The wavelength dependence of the coarse mode AOD was also modeled following T. F. Eck et al. (1999). We applied a climatology of the non-spherical dust phase function, derived from AERONET, to the coarse mode of the dust model to improve constraints on dust optical properties. It is worth noting that the non-spherical phase function was derived at 675 nm, and although the wavelength dependence of the phase function is relatively small (Fig. S3, <20%) across the DNB spectral bandpass, the disregard of phase function dependence on wavelength might later contribute to retrieval uncertainty.

For the fine mode of the dust aerosol model, our cluster analysis on AERONET observations indicated that the microphysics parameters, namely volume median radius, effective variance, and refractive index, showed less AOD dependence. Consequently, a set of fixed values, as listed in Table 1, were applied to UNL-VRTM which also allows utilizing MIE theory to calculate the required optical properties for radiative transfer simulation. The FMF was modeled as a function of AOD to dynamically assign weights when combining the coarse and fine mode into a single bi-modal dust aerosol model.

The configurations of the radiative transfer simulation were the same as illustrated in the Table 1 in Zhou et al. (2021) with slight modification on the representation of the surface reflectance to enable the utilization of the Cox-Munk BRDF model. Table 3 summaries those modifications, for detailed information of the simulation configurations, please refer to Table S3 or Zhou et al. (2021). Two 7-demensional normalized TOA radiance data cubes, t_{dust} and $t_{\text{sea salt}}$, (in dimension of $N_\tau \times N_{\text{mza}} \times N_{\text{vza}} \times N_{\text{sca}} \times N_\lambda \times N_{\text{ws}} \times N_{\text{LER}}$, where τ is the AOD and λ is the wavelength) were generated from the UNL-VRTM radiative transfer simulation. The dimension N_τ denotes the number of AOD values at 550 nm; N_{mza}, N_{vza}, and N_{sca} represent the numbers of discrete moon zenith angle, view zenith angle, and scattering angle, respectively; N_λ indicates the number of DNB sub-channels; N_{ws} is the number of wind speeds as the inputted of the Cox-Munk BRDF model; and N_{LER} is the number of discrete Lambertian surface reflectance (LER) values. To account the contribution of the Rayleigh scattering (<0.045) and gas absorption over the VIIRS DNB spectrum, we assumed a mid-latitude summer atmospheric profile with a surface pressure of 1013 mb in the UNL-VRTM simulation. We did not consider the impact of surface pressure variation on the Rayleigh scattering given the fact that molecular scattering is only a function of surface pressure and over the ocean surface the pressure variation is minimal (<4%, Singh and Aung, 2005). The variation of the water vapor was also neglected, since previous studies indicated VIIRS DNB is less sensitive to variation of water vapor (Wang et al., 2016).

Table 3
Modified configuration for generating LUTs.

Dimension Name	Variable Name in Table	Number of entries	Discrete Values
Surface reflectance	N_{LER}	4	0, 0.02, 0.04, 0.06
Wind Speed	N_{ws}	10	0.01, 0.5, 1, 4, 6, 8, 12, 16, 22, 30 m/s

Finally, the LUTs were obtained by convolving the simulated t (t_{dust} and $t_{\text{sea salt}}$ mentioned above) with DNB relative sensor response $f_{\text{RSR}}(\lambda)$ (RSR) and the moon irradiance database $E_{\text{1AU}}^{\text{TOA}}$ at each moonphase angle θ_p:

$$\rho_{\text{LUT}}(\tau,\mu,\mu_0,\psi,w_s,\rho_{\text{LER}},\theta_p) = \frac{\pi \int_{\lambda_2}^{\lambda_1} t(\lambda,\tau,\mu,\mu_0,\psi,w_s,\rho_{\text{LER}}) f_{\text{RSR}}(\lambda) E_{\text{1AU}}^{\text{TOA}}(\lambda,\theta_p)\, d\lambda}{\mu_0 \int_{\lambda_2}^{\lambda_1} f_{\text{RSR}}(\lambda) E_{\text{1AU}}^{\text{TOA}}(\lambda,\theta_p)\, d\lambda} \tag{1}$$

where, $E_{\text{1AU}}^{\text{TOA}}(\lambda,\theta_p)$ is the moon irradiance database normalized to one astronomical unit, developed by Miller and Turner (2009); it is dependent on the wavelength λ and moon phase angle θ_p. The numerator $\int_{\lambda_2}^{\lambda_1} t(\lambda,\tau,\mu,\mu_0,\psi,w_s,\rho_{\text{LER}}) f_{\text{RSR}}(\lambda) E_{\text{1AU}}^{\text{TOA}}(\lambda) d\lambda$ represents the simulated reflected lunar radiance received by the DNB at TOA; $\int_{\lambda_2}^{\lambda_1} f_{\text{RSR}}(\lambda) E_{\text{1AU}}^{\text{TOA}}(\lambda,\theta_p) d\lambda$ is the standard extraterrestrial lunar flux weighted by VIIRS DNB RSR. μ is the cosine of the view zenith angle, μ_0 is the cosine of the lunar zentih angle, Ψ is the relative azimuth angle, w_s is the wind speed, and the ρ_{LER} is the LER, respectively.

3.2. Derivation of the DNB TOA reflectance

Following Zhou et al. (2021), the TOA DNB reflectance is calculated through,

$$\rho_{\text{Meas}}^{\text{TOA}} = \frac{\pi I_{\text{DNB}}}{\mu_0 G_t \int_{\lambda_2}^{\lambda_1} f_{\text{RSR}}(\lambda) E_{\text{1AU}}^{\text{TOA}}(\lambda,\theta_p) d\lambda} \tag{2}$$

where I_{DNB} is the sensor sensed panchromatic radiance at the TOA in a unit of $\text{Wm}^{-2}\,\text{sr}^{-1}$; and G_t is a time dependent celestial adjustment factor determined by the Sun-Earth-Moon geometry. For more detailed derivation, please refer to Zhou et al. (2021) and Miller and Turner (2009). It is worth noting that although the radiance measured by the VIIRS DNB resonates with the moon phase, the TOA reflectance obtained via Eq. (2) exhibits less dependence on the moon phase.

3.3. Cloud, dust, and moon glint masking

While the NOAA/NASA VIIRS teams routinely produce standard operational cloud mask products for both S-NPP and NOAA-20 nighttime observation (CLDMSK), it has been noted that the cloud mask algorithm may misidentify the optically thick dust plumes as clouds. As an example, on 7 June 2020, a significant dust intrusion from the Sahara

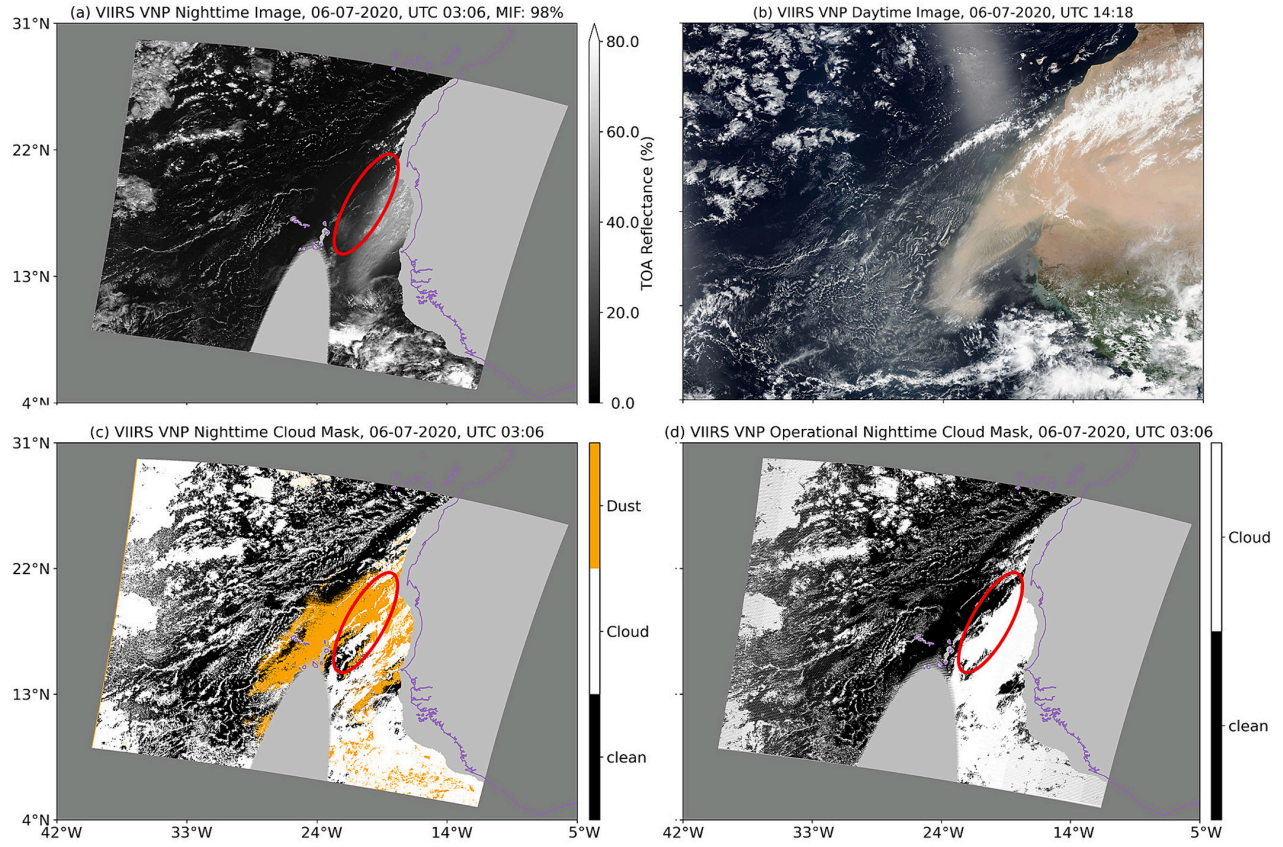

Fig. 2. An example of the internal cloud/dust mask of NOARA and the comparison with the standard product. (a) VIIRS DNB TOA reflectance on June 07, 2020, 0306 UTC over the North Atlantic Ocean. (b) VIIRS daytime true-color image for the same area of (a) but was observed at 1418 UTC; (c) The internal cloud and dust mask obtained by NOARA for the granule of the observation of (a); (d) the NASA operational cloud mask product for the granule of the observation of (a). The moon illumination fraction (MIF) of the observation is 98%. The red circle highlights the area where the standard cloud mask algorithm is misclassified as clouds. (For interpretation of the references to color in this figure legend, the reader is referred to the web version of this article.)

was evident over the North Atlantic. The location and the morphology of this event was readily captured in both the VIIRS DNB nighttime image (Fig. 2a) at 0306 UTC and the daytime true-color image (Fig. 2b) at 1418 UTC. However, the operational VIIRS cloud mask product not only misclassified this dust layer as clouds, but also incorrectly identified adjacent areas (the ocean northeast of Cape Verde, highlighted by the red circle) where no clouds were visible.

This misclassification can be attributed to two factors. First, the presence of dust in the atmosphere can lead to a reduction in the 10.76 μm brightness temperature (BT_{11}^{M}) and the 12 μm brightness temperature (BT_{12}^{M}) (Al-Shehhi, 2022; Dunion & Velden, 2004; Sokolik, 2002; Sun et al., 2019). It further causes underestimation of sea surface temperature (SST) derived from model simulations and real-time IR observations of BT_{11}^{M} and BT_{12}^{M}. The degree of reduction and underestimation varies with dust loading and dust composition. Consequently, this introduces significant uncertainty in estimating the temperature difference between the derived SST and BT_{11}^{M}, affecting the reliability of the surface temperature test. Additionally, clouds and dust affect the 8.6 μm brightness temperature ($BT_{8.6}^{M}$) in different ways, creating ambiguity in the results of the brightness temperature difference test, which contrasts $BT_{8.6}^{M}$ with BT_{11}^{M} observation, especially when a fixed threshold is applied in situations where both dust and cloud are present.

To mitigate this issue, in NOARA, a customized clouds mask is performed utilizing observations of the DNB, M-band, and I-band, based on the fast multi-channel mapping technique developed by Zhou et al. (2023). Detailed information on the cloud tests can be found in Table S1 in the supplementary materials. In addition to the cloud mask, NOARA incorporates two dust-pixel restoral tests (Table S2), following the methodology of Ackerman (1997). This cloud/dust masking allows NOARA to discard pixels affected by clouds while preserving, to some extent, those impacted by dust. We evaluated the NOARA CM with NASA operational cloud mask (OP CM) and CALIOP classifications for dust season (June, July, and August) of 2020 and 2021. The evaluation results are reported in Table S4 to Table S5. The results show a general agreement between the NOARA CM and OP CM. The NOARA CM aligned with OP CM in 93.41% of instances. 1.18% of pixels deemed cloudy by OP CM were seen as clean by NORRA CM. 5.41% of pixels identified as contaminated (cloudy or dusty) pixels by NOARA CM were classified as cloud-free by OP CM. The key differences arise from our algorithm's ability to identify dust pixels (1.46% mistaken for clouds by OP CM as the example shown Fig. 2) and to detect subpixel clouds using high-resolution I-band observations (2.68%) from those pixels identified as clean pixels by OP CM. Comparison against CALIOP further proves

that due to the usage of the DNB, the I-band high resolution observation, and internal dust tests, the misclassification was mitigated and the hit rate (for cloud-free aerosol-retrievable and cloudy pixels) was slightly increased to 91.97%, as compared to 90.3% hit rate of OP algorithm.

However, it is important to note that the low, optically thin stratus clouds can exhibit spectral and spatial signatures similar to aerosols such as dust and smoke, complicating the task of cloud mask algorithms to accurately differentiate between clouds, dust, and clean background using fixed thresholds. Regardless of the thresholds chosen, errors of omission and commission are likely to occur. Thus, a significant source of uncertainty in the NOARA algorithm stems from the potential omission of cloudy pixel. Lastly, moon glint regions are identified in this step, following a similar procedure to the sun glint test as outlined by Levy et al. (2013).

3.4. Retrieval of the oceanic AOD

The process of inverting the AOD from the DNB TOA reflectance ultilizes the re-calculated LUTs based on UNL-VRTM (Section 3.1). It involves two stages. In stage one, we employed linear interpolation to adjust the LUTs based on the moon phase angle, wind speed, and GOME-2 surface reflectance of the target pixel. Subsequently, we applied bilinear interpolation for the moon and sensor zenith angle, and linear interpolation for the scattering angle. These steps facilitated the derivation of LUTs tailored to a specific moon illumination, surface boundary condition, and view geometry; In the second stage, we employed the interpolated maritime LUT on cloud-free pixels to acquire an initial guess of their AODs. Then, for pixels whose initial AOD estimates exceed 0.25 or who were flagded as dust-affected, we used the interpolated dust LUT to invert their final AOD values.

At second stage, to further enhance the SNR, a 3 by 3 spatial window was utilized to acquire clean pixels and smooth the TOA reflectance. The retrieval process would only proceed when the number of valid pixels exceeded four, as shown in Fig. 1. Given the 750 m spatial resolution of the DNB, the spatial variation of aerosols within this approximately 2 by 2 km spatial window should be relatively minimal. It was anticipated that using more pixels for reflectance smoothing would reduce the retrieval error.

It is also important to note that additional radiance from gas flaring, ship lights, and other biogenic illumination sources over the ocean could increase the radiance signals received by the VIIRS DNB, thereby affecting the retrieved AOD. In NOARA, pixels affected by gas flaring are excluded using a yearly updated gas flaring database. However, due to the static nature of the database, some residuals are expected. Furthermore, while several studies have demonstrated the viability of the VIIRS DNB in detecting ship lights and biogenic illuminations over the sea, the automation of these detections is still in development. As a result, a positive bias in AOD is anticipated when surface illumination is present. One of the future developments for NOARA will be the rapid masking of these surface illumination sources to achieve more reliable AOD retrievals.

4. Retrieval demonstration and accuracy assessment

Several dust events over the North Atlantic Ocean's dust corridor (connecting NW African to the Caribbean Sea) are selected to demonstrate the performance of the NOARA algorithm. The first event took place from 5 June to 10 June 2020, serving as a prelude to the gigantic Godzilla Dust Storm over the North Atlantic Ocean for the year of 2020, the most severe episode in the past two decades (Yu et al., 2021). The second event encompassed the entire dust season of 2021, during which time, the AERONET frontline at Cape Verde had a moon photometer deployed to retrieve the nighttime AOD through its moonlight measurements, providing a valuable data source for the quantitative monitoring and evaluation of dust AOD at night. It is worth noting, while NOARA is applied across all sea regions, we exclude the coastal regions in statistical comparisons against AERONET and CALIOP.

4.1. Event 1: 2020 dust intrusion

Fig. 3 shows the satellite observations of the first dust intrusion event. The first column displays the DNB nighttime grayscale TOA reflectance, while the second column provides the corresponding daytime true-color images from the following afternoons. Overall, the MIF varied from 100% to 79%, providing ample illumination for VIIRS DNB to sense the dust over the ocean. Fig. 4 exhibits the AOD retrieved based on observations depicted in Fig. 3. The first column of Fig. 4 presents the NOARA AOD in this work retrived from the reflected moonlight sensed by VIIRS DNB, while the second column shows the VIIRS daytime DB AOD (VDB). Other AOD retrievals, such as from the MODIS DT algorithm (MDT, 3 km resolution), VIIRS DT algorithm (VDT), and the IASI IR AOD retrievals (IIR), are provided in Fig. S4 to Fig.S6, respectively. We've empirically set the upper bound of IIR at 1.25 for better visualization, as previous studies indicated that there is no universal and consistent scaling factor for converting the IIR (retrieved at a wavelength of 10 μm) to the visible AOD at 550 nm (Peyridieu et al., 2013). Clearly, the DNB retrievals align well with both the daytime visible AODs from MODIS and VIIRS and the IIR in terms of spatial distribution, and NOARA AOD values are also consistent with the VDB values in magnitude.

Beyond the general agreements between DNB and other AOD products, such high observational frequency (6–8 h per day) and continuity in the spatial distribution of AOD over time provide insights into the evolution and the horizontal movement of the dust plume. Seen from space, the genesis of the dust intrusion started on 6 June 2020, with low AOD values retrieved from the DNB at night (0142 to 0512 UTC, shown as Fig. 4a). Six hours later, IASI observed a large amount of the dust moving from the inland of Mauritania to its coastline (Fig. S6a). Unfortunately, MODIS Terra AOD retrieval around 1130 UTC could not capture this intrusion due to the sun glint.

Subsequently, as indicated by the sharp increase in AOD values retrieved from the early afternoon observations of VIIRS and MODIS, the heavy dust plume emitted from the western Sahara and transported further southwestward into the North Atlantic Ocean in the early morning around 1330 UTC (Fig. 4e, Fig. S4e, and Fig. S5a). The dust plume reached its peak strength on the 7 June, evident in the AOD retrievals by DT, BT as well as NOARA algorithms (shown as Fig. 4b for NOARA AOD, Fig. 4f for VDB, Fig. S4b for Terra MDT around 1130UTC, and Fig. S4f for Aqua MDT around 1430 UTC, Fig. S5b for VDT around 0230 UTC, and Fig. S6 c & d for IIR around 1000 and 2200 UTC, respectively).

A hook-shaped dust plume can be clearly discerned on the NOARA AOD map (Fig. 4b). In the following 24 h, this dust plume largely maintained its hook shape as seen by the daytime MDT (Fig. S4 b & f) and VIIRS AOD (Fig. 4f and Fig. S5b), and the IIR (Fig. S6 c & d). Interestingly, however, the NOARA AOD map around 0124 to 0436 UTC suggests that the dust plume broke into two segments on 8 June 2020 (Fig. 4c), a division not apparent in the AOD map retrieved by other algorithms prior to that NOARA AOD snapshot. This bifurcation of dust plumes can be confirmed by other AOD retrievals in the daytime and IR bands in the following morning and afternoon on 8 June 2020. More interestingly, by simply tracking the front of the transported segment of the dust ("hook tip"), an average wind speed could be roughly estimated. Shown as Fig. 5, on 8 June 2020, NOARA AOD indicates that the "hook tip" of the dust plume was around 10.77° N, 25.6° W. About 12 h later, VDB shows the dust front moved southwestward to 10.79° N,

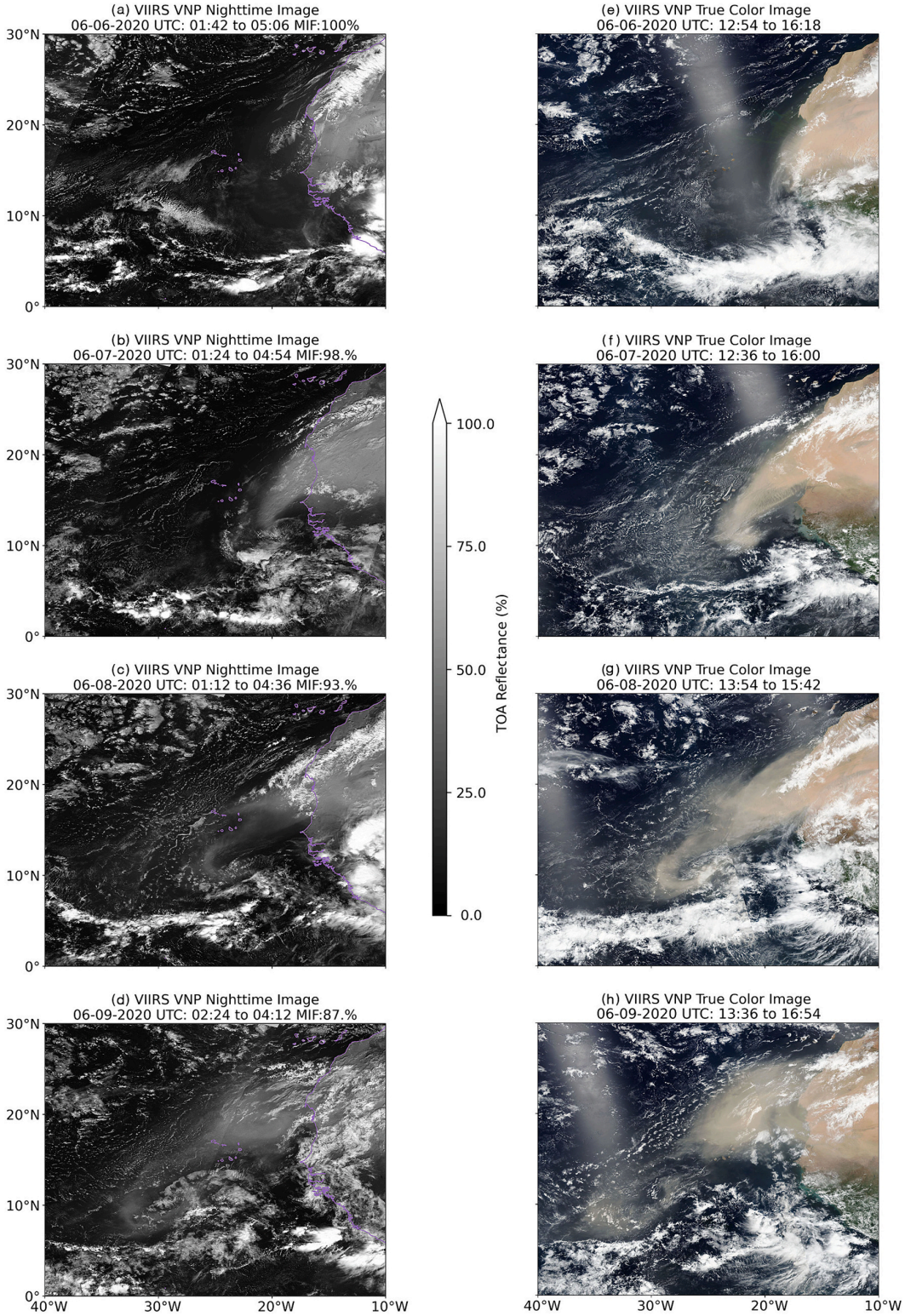

Fig. 3. Satellite images over the North Atlantic Ocean from 6 June to 9 June 2020 sensed by the S-NPP VIIRS. (a) – (d) Nighttime DNB gray scale TOA reflectance. (e) – (h) Daytime true-color images. VNP stands for the VIIRS S-NPP.

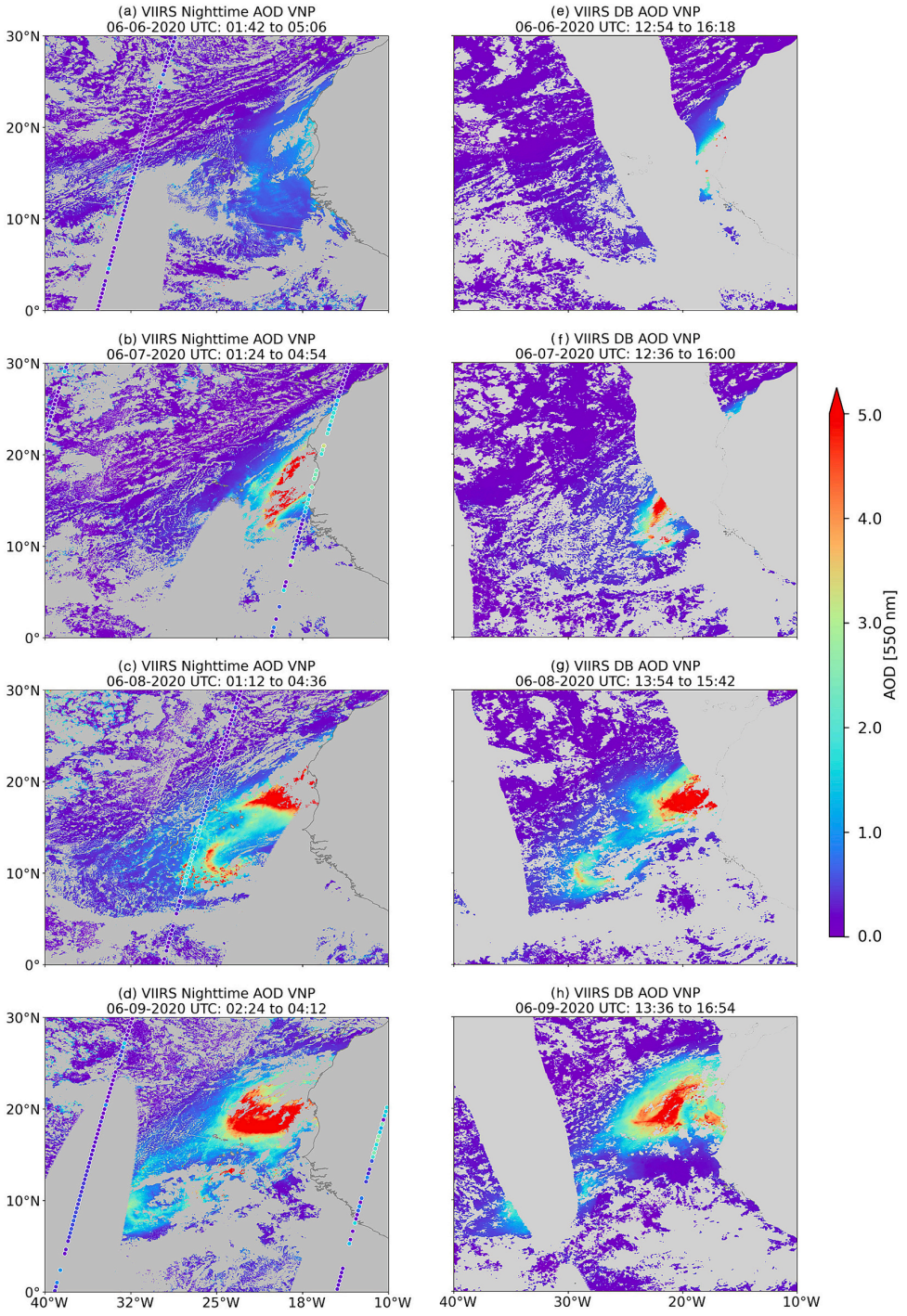

Fig. 4. AOD retrieval over the North Atlantic Ocean from 6 June to 9 June 2020. (a) – (d) Nighttime AOD retrieved by VIIRS DNB reflected moonlight. (e) – (f) VIIRS Daytime DB product. The color-coded trajectories on the nighttime AOD map are the CALIOP AOD. VNP stands for VIIRS S-NPP.

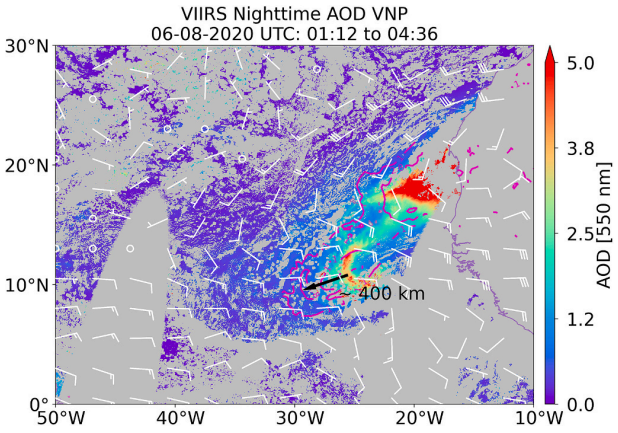

Fig. 5. A close look at the dust transport on 8 June 2020. The color map is the DNB AOD retrieved from 0242 to 0436 UTC. The magenta contour delineates the 'hook tip' seen by the VIIRS DB AOD in the following afternoon on 9 June 2020 at 1542 UTC. The wind speed information comes from the MERRA-2 assimilated meteorological fields (M2I3NPASM). It is the averaged wind speed from 650 to 750 hPa levels. The black arrow denotes the direction of the "hook tip" movement. In ~12 h, it moved around 400 km. VNP stands for VIIRS S-NPP.

29.09° W, as indicated by the magenta contour in Fig. 5. The distance for the movement is approximately 400 km, resulting in an average wind speed of 33.6 km h^{-1}, which is consistent with the 12-h wind speed average of 32.9 km h^{-1} between 650 and 750 hPa levels in MERRA-2 assimilated meteorological fields data.

To further validate the DNB AOD retrieval quantitatively, DNB AOD is compared with the AOD retrieved from CALIOP. On 8 June 2020, CALIOP overpassed the west coastline of North Africa, providing a glimpse of the dust plume. Fig. 6 compares the DNB AOD (retrieved with a MIF up to 90%) against the CALIOP AOD. Fig. 6a is the CALIOP level-2 total attenuated backscattering coefficient curtain plot on 8 June 2020. CALIOP observation revealed a noticeable heavy scattering layer spanning from 23° N to 6° N and extending up to 5 km above the sea surface. The attenuated backscattering reached up to 0.1 km^{-1} sr^{-1}. The standard CALIOP feature mask (shown in Fig. S8) confirmed that this lofting layer primarily consists of dust particles. The DNB and CALIOP AODs are denoted as the orange and white lines on the backscattering plot, respectively. Spatially, the DNB retrievals captured the spatial gradient of the dust plume seen by the CALIOP from north to south effectively. Fig. 6b shows a scatter plot comparing the collocated DNB and CALIOP AODs. The black data pairs are the collocated DNB and CALIOP AODs from those retrievable nights of the first dust events (from June 5th to 10th 2020), while the orange data pairs are specific for the 8 June 2020. Statistically, the τ_{DNB} is highly correlated with the τ_{CN} with a high R value up to 0.97 on 8 June 2020. Approximately 73.44% of the pairs fall into the uncertainty envelope defined as $10\%\tau_{DNB} + 0.085$, bolstering confidence in the DNB AOD retrieval quality. More data pairs (77.34%) fall into the defined uncertainty envelope for the entire case studies since τ_{DNB} match even better with τ_{CN} when AOD is small. The outliers, indicating the overestimating of the AOD, are likely caused by the cloud edge where the subpixel cloud cannot be perfectly removed.

The scientific merit of the NOARA retrieval lies in its potential ability to further constrain the forecast and reanalysis of the chemical transport models (CTMs) to produce more realistic products. Fig. 7 presents AOD retrievals at the IASI nighttime (2200 UTC) overpass on June 06, VIIRS midnight (0130 UTC), IASI daytime (1000 UTC), MODIS Terra (1130 UTC), and Aqua overpass (0130 UTC) overpass on June 07, as well as the nearest MERRA-2 aerosol reanalysis counterparts for VIIRS and MODIS retrievals for both daytime and nighttime, respectively. For a time series (3-h interval) of the MERRA-2 AOD for the entire event, please refer to Fig. S7. It is evident that MERRA-2 first captured the genesis of the dust intrusion (Fig. S7(1)) when compared with the DNB AOD (Fig. 4a). However, it significantly underestimated the development of the dust loading (e.g., showing bias low in AOD) and relied on the assimilation of MODIS observation (not the MDT or MDB AOD, but a Neural Network based AOD translated from the MODIS radiance to AERONET-calibrated AOD; developed by Global Modeling and Assimilation Office) (Randles et al., 2017) to correct the mass concentration of the dust in the plume, as demonstrated by the sharp AOD increase from 1200 to 1500 UTC on 6 June 2020 (Fig. S7(5)).

After the daytime data assimilation at 1500 UTC on 6 June 2020, however, the model (Fig. 7f) diverged from the subsequent satellite observations at midnight (Fig. 7b) and produced unrealistic results in

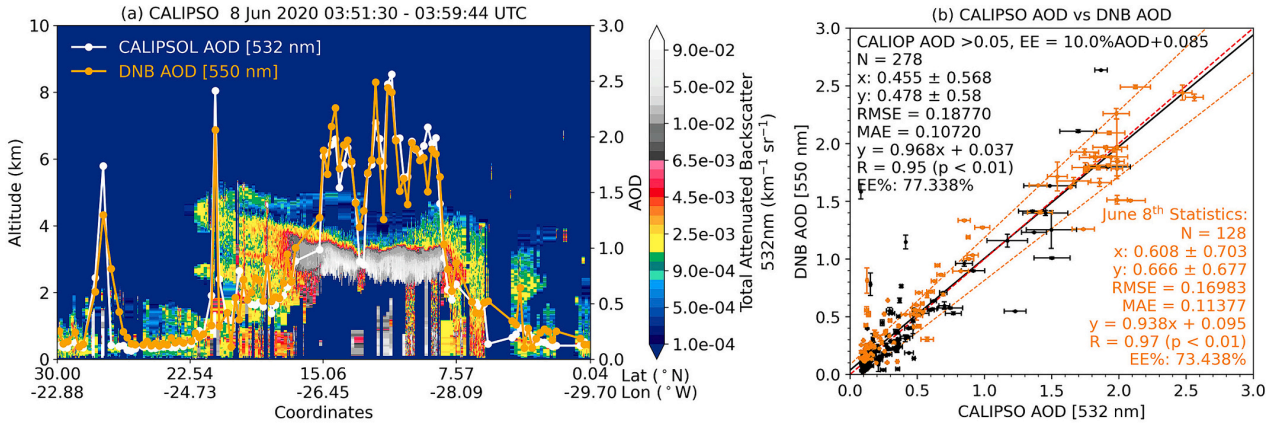

Fig. 6. Comparison of DNB AOD with the CALIPSO-CALIOP AOD. (a) CALIOP level 3 backscattering image (5 km resolution) overlaid with AOD (right y-axis) from NOARA and CALIOP (orbit number 75100), (b) Scatter plot of CALIOP AOD with NOARA AOD. The error bars represent the standard deviation of the available CALIOP/DNB retrievals within 50 km diameter. The red broken line is the one-to-one line; the best regression line is obtained through least square and denoted as the black solid line; the error envelopes are defined as ± (0.085 + 10% AOD) and denoted as the orange broken lines. The black dots in (b) represent the collocated AOD pairs from the retrievable nights of the first dust events from 5 June to 10 June 2020, with corresponding statistical summaries provided in black text. The orange dots denote collocated AOD pairs on 8 June 2020, and the statistical summaries are in orange text. (For interpretation of the references to color in this figure legend, the reader is referred to the web version of this article.)

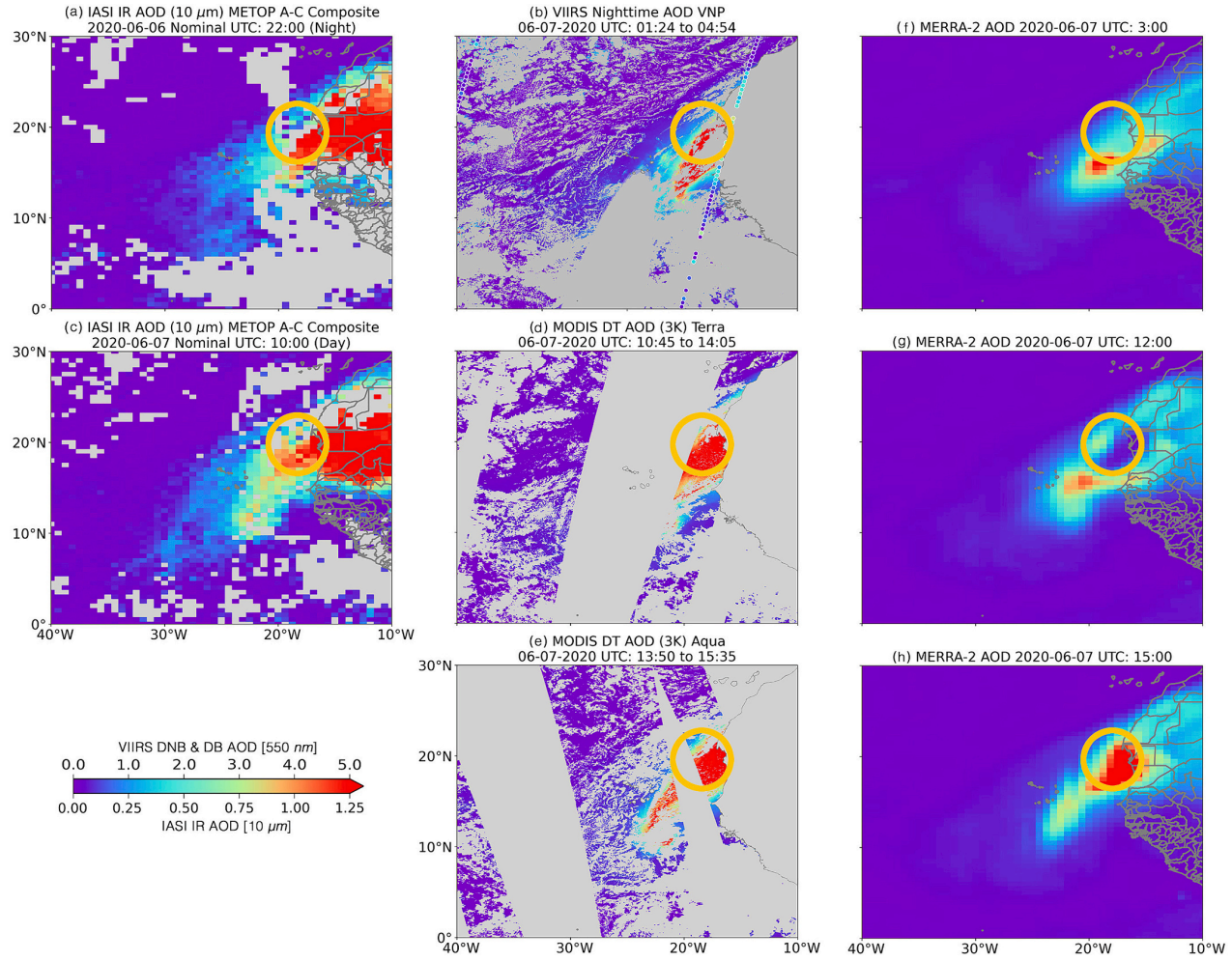

Fig. 7. Satellite AOD time series of the abnormal MERRA-2 AOD lost event on 7 June 2020. (a) IASI dust IR AOD retrieval at 2200 UTC on 6 June 2020; (b) VIIRS DNB AOD retrieval at 0300 UTC on 7 June 2020; (c) IASI dust IR AOD retrieval at 1000 UTC on 7 June 2020; (d) MODIS Terra DT AOD at 1045 UTC on 7 June 2020; (e) MODIS Terra DT AOD at 1350 UTC on 7 June 2020; (f) – (h) MERRA-2 AOD simulation at 0300, 1200 and 1500 UTC on 7 June 2020, respectively. VNP stands for VIIRS S-NPP.

the following 24 h shown in Fig. S7(7) to S7(13), when compared to this study's DNB AOD (Fig. 7b), MDT (Fig. 7d and Fig. 7e), and IIR (Fig. 7a. and Fig. 7c). Specifically, the model simulation from 6 to 7 June 2020 (Fig. S7(7) to Fig. S7(12)) depicts a gradual decrease of the AOD over the coastal area of Mauritania, implying a significant sink or deposition of dust particles in model. Particularly, in the early morning of 7 June 2020, as marked by the orange circle, a noticeable cool spot is shown on the MERRA-2 AOD map (Fig. 7g), contradicting the MODIS Terra AOD shown in Fig. 7d. The pattern was corrected in the MERRA-2 simulation after 1500 UTC, when MODIS Aqua AOD was assimilated into the system.

While determining the exact reason for the AOD decrease on 1200 UTC for MERRA-2 is beyond the scope of this manuscript, it is plausible that the model would have performed better if data assimilation incorporating NOARA information into the model had been conducted at midnight. Hence, the case illustrates one of the key advantages of gap-filling nocturnal AOD such as NOARA in terms of rendering more accurate aerosol reanalysis for myriad downstream applications.

4.2. *Event 2: 2021 dust season*

In 2021, the number of AERONET nighttime sites deployed over the Atlantic Ocean increased to seven, providing more reliable ground-based AOD observations for validating the NOARA. We expanded the retrieval domain westward to 100° W and northward to 40° N, encompassing the entire North Atlantic Ocean, and conducted retrievals for the full dust season from June to August. Considering factors such as episodic dust events, moon illumination, and view geometry, a total of 18 days were deemed suitable for showcasing the capabilities of NOARA across the Atlantic. A significant dust event in August 2021, depicted in Fig. 8, was selected for detailed illustration. The comparison of NOARA AOD with CALIOP backscattering for this event, specifically on Aug. 23, is presented in Fig. S9, focusing on both heavy dust layers and thin dust transport. As shown in Fig. 8, NOARA effectively captured the onset, progression, and dispersion of the dust intrusion. Notably, when juxtaposed with the CALIOP backscattering images, NOARA's proficiency in mapping the spatial distribution of dust transport becomes evident. This

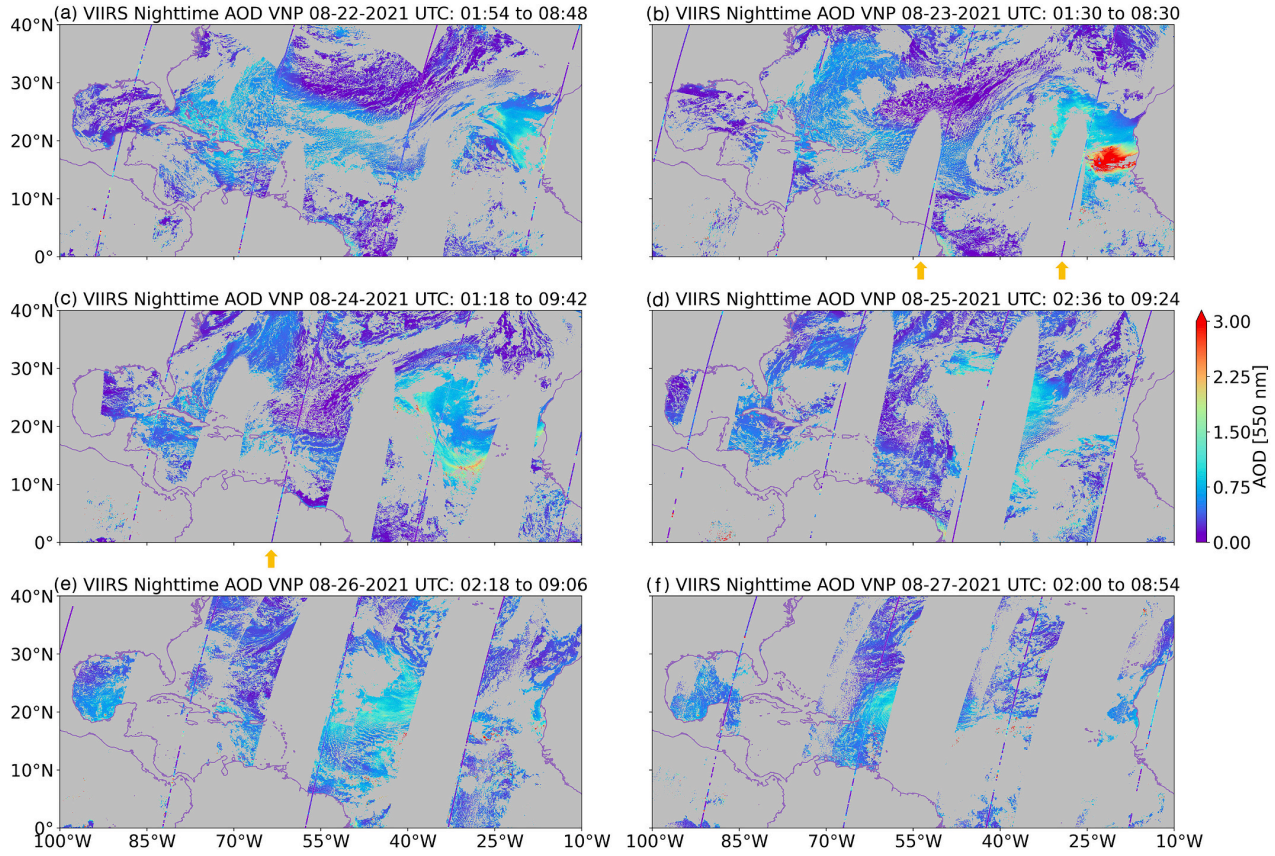

Fig. 8. DNB AOD retrievals over the Atlantic Ocean for August 2021. The dotted lines are the CALIOP trajectories colored coded with the AOD retrievals at 532 nm. Please refer to Fig. S9 for CALIOP comparison for trajectory highlighted by orange arrows.

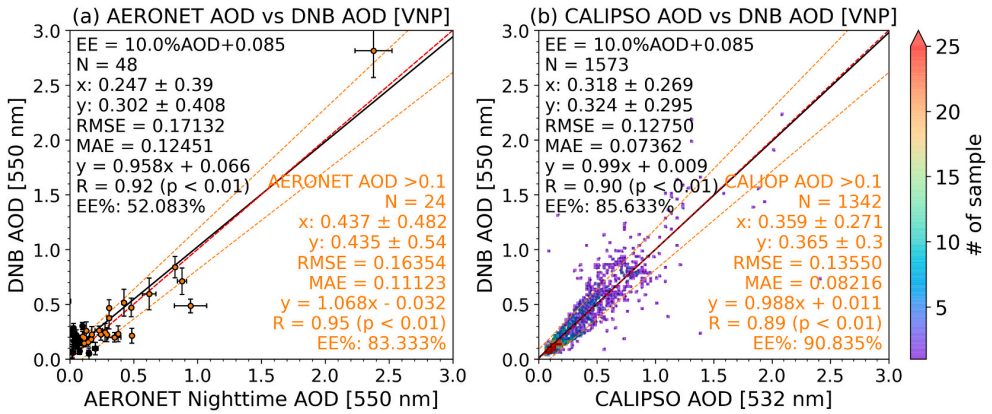

Fig. 9. Statistical comparison of the DNB AOD with multiple AOD retrievals for the whole dust season (June to August 2021). (a) Comparison of the AERONET Lunar AOD with the DNB AOD. (b) Comparison of the CALIOP nighttime AOD with the NOARA AOD. The error bars represent the standard deviation of the available CALIOP/DNB/AERONET retrievals within 50 km diameter. The red broken line is the one-to-one line; the best regression line is obtained through least square and denoted as the black solid line; the error envelopes are defined as ± (0.085 + 10% AOD) and denoted as the orange broken lines. The statistics provided in orange colors are for AERONET and CALIOP AODs that are >0.1. VNP stands for VIIRS S-NPP. (For interpretation of the references to color in this figure legend, the reader is referred to the web version of this article.)

is observable in areas with heavy dust concentration (AOD > 1) as well as in downwind transport sectors where dust is less dense (AOD < 1).

Fig. 9 shows the scatter plots comparing the AERONET AOD and CALIOP AOD with the S-NPP NOARA AOD from June to August 2021, respectively. In general, NOARA AODs were consistent with those measurements taken at night by both AERONET and CALIOP. Interestingly, when $\tau_{LNR} > 0.1$, the NOARA AOD shows a better agreement with the AERONET with an R value of 0.95 and an EE ratio of 83.3%. Upon closer examination of those τ_{LNR} and τ_{DNB} pairs that have $\tau_{LNR} < 0.1$, we found that ~95% of the pairs show an overestimation of NOARA AOD

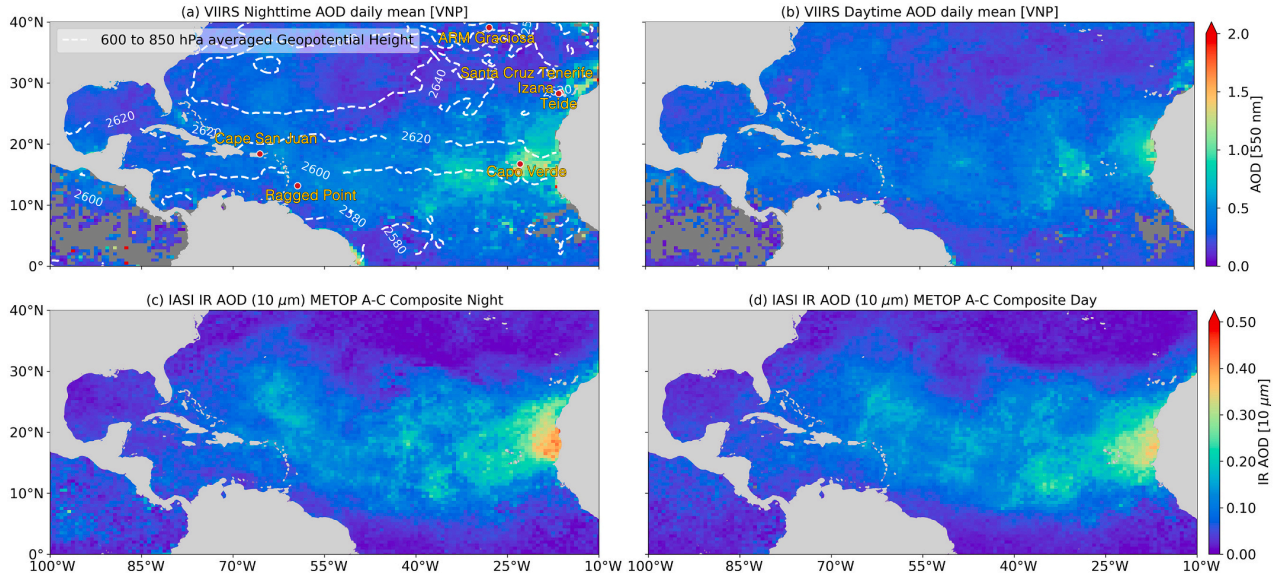

Fig. 10. Illustration of the DNB retrieval climatology for dust season of 2021 (June, July and August). (a) Daily mean of the DNB retrievals; (b) Daily mean of the VIIRS DB retrievals; (c) Daily mean of the IASI nighttime retrievals; (d) Daily mean of the IASI daytime retrievals. The white broken lines (a) are the averaged geopotential height between 600 and 850 hPa. VNP stands for VIIRS S-NPP.

when compared against AERONET. However, this overestimation is not observed in the CALIOP and DNB comparison. This discrepancy is likely due to the representation of the surface reflectance over the coastline or turbid water. As those collocated AERONET sites are located on small islands, the current GOME-2 and Cox-Munk BRDF used in the retrieval might not adequately capture the variation in the surface reflectance over shallow water. In contrast, most of the CALIOP and DNB pairs are located in the deep ocean where the surface models are more effective in representing the surface reflectance.

We resampled the 18 days of NOARA AOD to the MERRA-2 grid to generate a nighttime dust AOD climatology over Atlantic for the year 2021, as shown in Fig. 10a. Even with this limited number of days averaged, an apparent east-to-west AOD gradient over the Atlantic emerges, indicating the gradual weakening of dust transport due to deposition. This nighttime climatology aligns with its daytime counterpart (Fig. 10b), averaged from the daytime VIIRS DB AOD retrievals for the same dates as the DNB retrievals. It is also consistent with the IR view of dust climatology generated from the IASI retrievals using the same sampling strategy, as shown in Fig. 10c and d. Noticeably, as shown by the DNB climatology and verified by others, the dust transport pattern is discernable, with the influence of dust extending up to 25°N over the dust source regions steered by the African Easterly Jet. Beyond this area, the impact tapers off. However, due to the robust trade winds and the strong Bermuda-Azores High, the dust impact can extend up to 35°N at the western terminus of the Atlantic.

The NOARA climatology also effectively outlines areas less impacted by dust, such as the Canary Basin and further west in the mid-Atlantic, as visible in the DB and IASI climatology. Despite the general agreement in portraying the spatial distribution of dust over the Atlantic, Fig. 11 offers a statistical comparison between these climatology. As depicted in Figs.11a and 11b, the NOARA AOD and VIIRS DB AOD climatology both exhibit positive correlations with the IASI nighttime and daytime IR AOD climatology, with correlation coefficients of 0.71 and 0.79 respectively, further confirming the consistency of these climatological outcomes.

It is worth noting that this daily mean of AOD is subject to the number of valid retrievals, as clouds may be present over certain regions more frequently for this short period of averaging. This limitation caused a slight discontinuity in the AOD map such as in Cape Verde area. Fig. S10a shows the number of AOD retrievals used in the averaging. Over the south of Cape Verde (Island Tiago), the total number of days having valid AOD was only four to six out of the 18 days, among which the DNB AOD reached 2.8 ± 0.24 (with AERONET measurement 2.37 ± 0.15) on 23 August 2023 when the heavy dust intruded the Atlantic Ocean. This high AOD value greatly boosted the daily mean, making AOD slightly greater than that of the Bay of Arguin, despite it being further west from the dust source. Nevertheless, the results presented here demonstrate the capability of the DNB retrievals in depicting the transport of dust at night.

5. Discussion and summary

In this work, we expanded on an algorithm developed by Zhou et al. (2021) which uses VIIRS DNB observations of reflected moonlight to retrieve AOD over the rural/wildland areas, extending it to cover ocean surfaces. New implementations introduced include: 1. Creating the new aerosol models to describe the optical properties of sea salt and dust particles for the nighttime VIIRS retrieval; 2. Integrating the Cox and Munk BRDF model to improve the representation of ocean surface reflectance; 3. Developing new internal cloud and dust masking schemes for more precise classification of the retrievable area. 4. Auto-adjusting the aerosol model from sea-salt to dust based on an initial AOD retrieval.

This algorithm enables the mapping of visible AOD over the Atlantic Ocean at night, offering full spatial coverage of dust transport. The retrievals were validated against multiple AOD measurements such as 550 nm daytime AOD from MODIS and VIIRS (using DT or DB algorithm), 10 μm AOD from IASI, 532 nm AOD from CALIOP measurement, and 550 nm AOD from the AERONET lunar observation. The validation revealed good consistency between the DNB AOD and these AOD measurements in terms of general spatial distribution and magnitude. Quantitative comparisons showed that DNB AOD positively correlates with AERONET nighttime AOD and CALIOP AOD with R-values of 0.95 and 0.89, respectively, thus shedding light on nocturnal dust transport.

The uncertainty associated with DNB retrievals has been comprehensively discussed in Zhou et al. (2021). Generally, the sources of uncertainty arise from the imperfect representation of lunar irradiance, VIIRS DNB calibration, surface representation, and the aerosol model. The uncertainties due to the lunar irradiance database and DNB

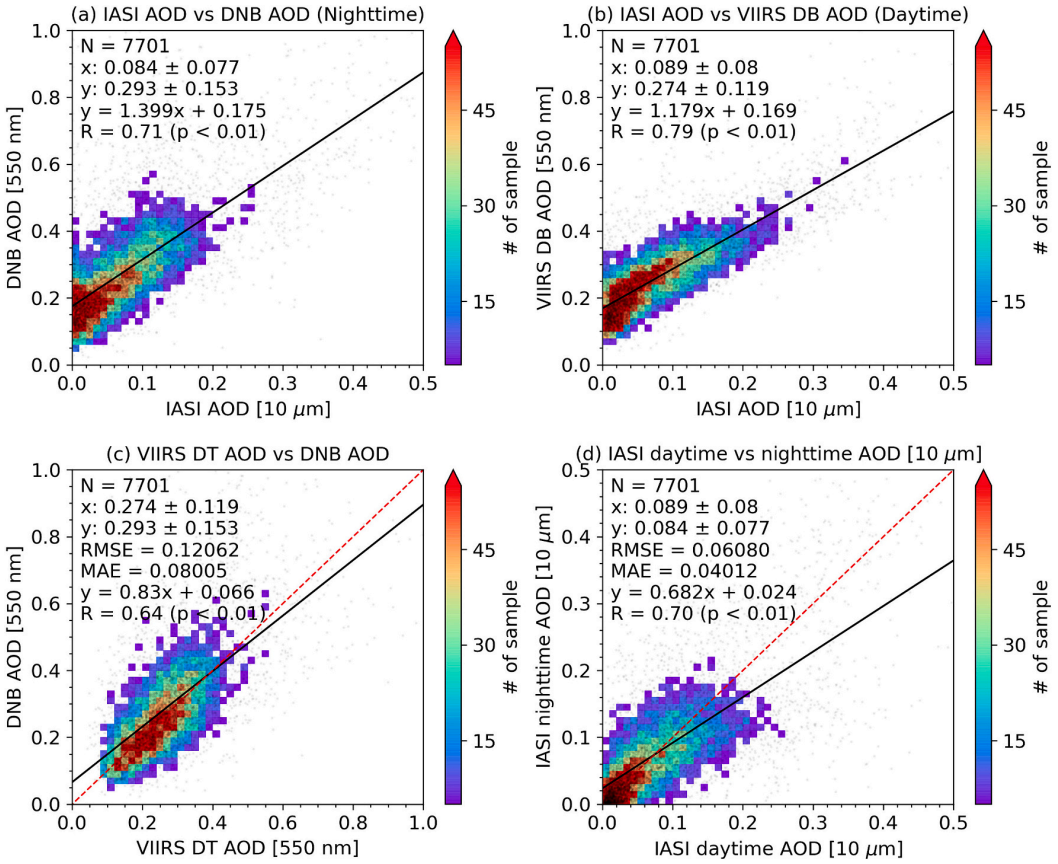

Fig. 11. Statistical comparison of the dust season climatology of 2021 derived from the three algorithms. (a) NOARA AOD at 550 nm vs. IASI nighttime AOD at 10 μm; (b) VIIRS DB AOD at 550 nm vs. IASI nighttime AOD at 10 μm; (c) NOARA AOD vs. Daytime VIIRS DB AOD; (d) IASI Daytime AOD vs. IASI nighttime AOD. The best regression is obtained through ordinary least squares and denoted as the black solid line; the red broken line is the one-to-one line. RMSE and MAE are not provided for (a) and (b) because they are different physical parameters. (For interpretation of the references to color in this figure legend, the reader is referred to the web version of this article.)

calibration are estimated to be <0.07 and 0.08, respectively. The uncertainty of the aerosol model is more complex. Our previous studies indicate that a variation in SSA of 0.03 can lead to an 8% uncertainty in AOD retrieval. The uncertainty related to surface reflectance is influenced by the error in MERRA-2 wind speed forecasts and the GOME-2 LER data. An uncertainty of 2 m/s in wind speed forecast, as documented by Carvalho (2019), can result in a change of <0.003 in surface reflectance for appropriate viewing geometries. Additionally, the GOME-2 LER data provide a statistical error analysis at each band, with uncertainties generally within 0.01 over the Atlantic Ocean. Overall, we estimate that the uncertainty in surface reflectance will contribute <0.006 to the AOD retrieval. Combining these factors, including those very small Rayleigh scattering and gas absorbtion discussed in Section 3.1, we anticipate an average uncertainty of 0.13 in AOD retrieval for this work, with a maximum potential uncertainty of 0.16. However, depending on the specific cases, the uncertainties from various sources may be random and could potentially offset one another. Therefore, the overall uncertainty estimated here represents an upper limit for quantifying the total uncertainty in the retrieval process. Comparisons with several independent datasets suggest an overall uncertainty (1-sigma) of 0.085 and an uncertainty envelope of 0.085 + 0.10AOD, within which at least 67% of (retrieval vs. referece) data pairs are expected to reside.

As a single channel algorithm, the NOARA algorithm must make assumptions about aerosol model and surface reflectance. While the parameterization of ocean surface reflectance over the deep ocean is well established, uncertainties remain for the coastal/shallow-water regions. Aerosol models also vary with time and season. As it stands, NOARA, in its research algorithm stage, has only developed a dust aerosol model and a background maritime model. The AOD-based segregation of the dust aerosol and the sea-salt aerosol is rudimentary. It is worth noting while the AOD threshold of 0.25 proves to be sufficient for the dust season, it could introduce uncertainties if applied to other seasons when dust is not the dominant aerosol present over the North Atlantic. For global retrieval purposes, more aerosol models need to be defined and methods to classify the aerosol types need to be further investigated.

The nighttime retrieval ability of VIIRS DNB is limited not only by the moon phase but also by Sun-Earth-Moon geometry, which is a function of time, location, and the overpass time of the sensor. Generally, for the North Atlantic Ocean during the Sahara dust season, an average of 6 days of retrievals per month is expected for the VNP's overpass time of 0130 LST. The retrieval ability might increase (up to ~10 days) for area near the equator where the moon zenith angle will be smaller for S-NPP overpass time. Regardless, the study in this paper underscores the capabilities of a nighttime low-light sensor in atmosphere aerosol sensing from the space, especially if more resources are added to bolster the temporal sampling capabilities across the nights (and capturing additional nights of the lunar cycle). This study, albeit with a limited number of case studies comparing with CTM outputs, underscores a notable gap inherently associated with the daytime-only aerosol data assimilation scheme in the CTM, which leads to rather limited capability in describing and capturing the complete diurnal

(daytime and nighttime) process of aerosol transport. The availability of high-quality global nighttime aerosol retrievals, especially if operational in near-real-time, could provide crucial information to bridge this observational gap. Such advancements would result in an improved initialization of nighttime aerosols conditions in CTM, therefore significantly enhance CTM's capabilities for forecasting and reanalysis of aerosol distributions.

Data available statament

The VIIRS L1B data is downloaded from https://ladsweb.modaps.eosdis.nasa.gov/. The MERRA-2 M2T3NVASM, M2I3NXGAS and M2T3NVASM download from https://gmao.gsfc.nasa.gov/reanalysis/MERRA-2/. The GOME-2 surface Lambert-equivalent reflectivity (LER) database is downloaded from. Nighttime ground AOD measurements from https://www.temis.nl/surface/albedo/gome2_ler.php. AERONET LUNAR AOD Version 3 PROVISIONAL is download from https://aeronet.gsfc.nasa.gov/cgi-bin/draw_map_display_aod_v3_lunar. The Version 4.10) CALIOP nighttime aerosol profile is downloaded from https://asdc.larc.nasa.gov/data/CALIPSO/. The daytime VIIRS Dark Target (AERDB_L2_VIIRS_SNPP), Deep Blue (AERDT_L2_VIIRS_SNPP) AOD, MODIS DT AOD (3 km resolution, MOD04 and MYD04) are downloaded https://ladsweb.modaps.eosdis.nasa.gov/.

The IASI Level 2 dust AOD retrieval is downloaded from https://iasi.aeris-data.fr/dust-aod_iasi_a_arch/. The retreival data presented in this study will be available at https://arroma.uiowa.edu/models.php upon request.

CRediT authorship contribution statement

Meng Zhou: Writing – review & editing, Writing – original draft, Visualization, Validation, Software, Resources, Project administration, Methodology, Investigation, Formal analysis, Data curation, Conceptualization. **Jun Wang:** Writing – review & editing, Supervision, Resources, Project administration, Funding acquisition, Conceptualization. **Xi Chen:** Writing – review & editing, Resources, Methodology, Formal analysis. **Yi Wang:** Writing – review & editing, Software, Formal analysis. **Peter R. Colarco:** Writing – review & editing, Resources, Formal analysis, Data curation. **Robert C. Levy:** Writing – review & editing, Resources, Formal analysis, Data curation. **Steven D. Miller:** Writing – review & editing, Software, Formal analysis.

Declaration of competing interest

The authors declare that they have no known competing financial interests or personal relationships that could have appeared to influence the work reported in this paper.

Data availability

Data will be made available on request.

Acknowledgement

This study was supported by NASA SNPP/JPSS/Terra/Aqua program (grant #: 80NNSC21K1976 and 80NSSC21K1981). Meng Zhou is supported by the support of Future Investigators in NASA Earth and Space Science and Technology (FINESST) program (grant #: 80NSSC21K1628). We express our gratitude for the open access to VIIRS data, provided by NASA's Earth Observing System Data and Information System (EOSDIS), as well as the CALIOP Level 2 aerosol profile data from NASA Langley Research Center's Atmospheric Science Data Center. Our appreciation extends to all Principal Investigators, Co-Principal Investigators, and respective team members for their efforts in setting up and maintaining the AERONET sites integral to this research. We also acknowledge atmospheric data and services center (AERIS) for their efforts to maintain the IASI dust AOD retrieval.

Appendix A. Supplementary data

Supplementary data to this article can be found online at https://doi.org/10.1016/j.rse.2024.114315.

References

Ackerman, S.A., 1997. Remote sensing aerosols using satellite infrared observations. J. Geophys. Res. Atmos. 102 (D14), 17069–17079.
Al-Shehhi, M.R., 2022. Uncertainty in satellite sea surface temperature with respect to air temperature, dust level, wind speed and solar position. Regional Studies in Marine Science 53, 102385.
Bao, F., Huang, K., Wu, S., 2023. The retrieval of aerosol optical properties based on a random forest machine learning approach: exploration of geostationary satellite images. Remote Sens. Environ. 286, 113426.
Buchard, V., Randles, C., Da Silva, A., Darmenov, A., Colarco, P., Govindaraju, R., et al., 2017. The MERRA-2 aerosol reanalysis, 1980 onward. Part II: evaluation and case studies. J. Climate 30 (17), 6851–6872.
Callewaert, S., Vandenbussche, S., Kumps, N., Kylling, A., Shang, X., Komppula, M., et al., 2019. The mineral aerosol profiling from infrared radiances (MAPIR) algorithm: version 4.1 description and evaluation. Atmospheric. Meas. Tech. 12 (7), 3673–3698.
Capelle, V., Chédin, A., Siméon, M., Tsamalis, C., Pierangelo, C., Pondrom, M., et al., 2014. Evaluation of IASI-derived dust aerosol characteristics over the tropical belt. Atmos. Chem. Phys. 14 (17), 9343–9362.
Carvalho, D., 2019. An assessment of NASA's GMAO MERRA-2 reanalysis surface winds. Journal of Climate 32 (23), 8261–8281.
Chen, X., Wang, J., Xu, X., Zhou, M., Zhang, H., Garcia, L.C., et al., 2021. First retrieval of absorbing aerosol height over dark target using TROPOMI oxygen B band: algorithm development and application for surface particulate matter estimates. Remote Sens. Environ. 265, 112674.
Chen, X., Wang, J., Gomes, J., Dubovik, O., Yang, P., Saito, M., 2022. Analytical prediction of scattering properties of spheroidal dust particles with machine learning. Geophys. Res. Lett. 49 (9) e2021GL097548.
Christopher, S.A., Wang, J., Ji, Q., Tsay, S.-C., 2003. Estimation of diurnal shortwave dust aerosol radiative forcing during PRIDE. J. Geophys. Res. Atmos. 108 (D19) https://doi.org/10.1029/2002JD002787.
Clarisse, L., Clerbaux, C., Franco, B., Hadji-Lazaro, J., Whitburn, S., Kopp, A., et al., 2019. A decadal data set of global atmospheric dust retrieved from IASI satellite measurements. J. Geophys. Res. Atmos. 124 (3), 1618–1647.
Cox, C., Munk, W., 1954. Measurement of the roughness of the sea surface from photographs of the sun's glitter. Josa 44 (11), 838–850.
De Paepe, B., Dewitte, S., 2009. Dust aerosol optical depth retrieval over a desert surface using the SEVIRI window channels. J. Atmos. Oceanic Tech. 26 (4), 704–718.
Di Noia, A., Hasekamp, O.P., Wu, L., van Diedenhoven, B., Cairns, B., Yorks, J.E., 2017. Combined neural network/Phillips–Tikhonov approach to aerosol retrievals over land from the NASA research scanning Polarimeter. Atmos. Meas. Tech. 10 (11), 4235–4252.
Dunion, J.P., Velden, C.S., 2004. The impact of the Saharan air layer on Atlantic tropical cyclone activity. Bulletin of the American Meteorological Society 85 (3), 353–366.
Eck, T.F., Holben, B.N., Reid, J.S., Dubovik, O., Smirnov, A., O'Neill, N.T., et al., 1999. Wavelength dependence of the optical depth of biomass burning, urban, and desert dust aerosols. J. Geophys. Res. Atmos. 104 (D24), 31333–31349. https://doi.org/10.1029/1999JD900923.
Elvidge, C.D., Zhizhin, M., Hsu, F.-C., Baugh, K.E., 2013. VIIRS nightfire: satellite pyrometry at night. Remote Sens. (Basel) 5 (9), 4423–4449.
Elvidge, C.D., Baugh, K., Zhizhin, M., Hsu, F.C., Ghosh, T., 2017. VIIRS night-time lights. Int. J. Remote Sens. 38 (21), 5860–5879. https://doi.org/10.1080/01431161.2017.1342050.
Fan, C., Fu, G., Di Noia, A., Smit, M., Rietjens, H.H., J, A., Ferrare, R., et al., 2019. Use of a neural network-based ocean body radiative transfer model for aerosol retrievals from multi-angle polarimetric measurements. Remote Sens. (Basel) 11 (23), 2877.
Fu, D., Xia, X., Duan, M., Zhang, X., Li, X., Wang, J., Liu, J., 2018. Mapping nighttime PM2.5 from VIIRS DNB using a linear mixed-effect model. Atmos. Environ. 178, 214–222. http://www.sciencedirect.com/science/article/pii/S1352231018300736.
Gao, M., Franz, B.A., Zhai, P.-W., Knobelspiesse, K., Sayer, A.M., Xu, X., et al., 2023. Simultaneous retrieval of aerosol and ocean properties from PACE HARP2 with uncertainty assessment using cascading neural network radiative transfer models. Atmos. Meas. Tech. 16 (23), 5863–5881.
Gelaro, R., McCarty, W., Suárez, M.J., Todling, R., Molod, A., Takacs, L., et al., 2017. The modern-era retrospective analysis for research and applications, version 2 (MERRA-2). J. Climate 30 (14), 5419–5454.
Getzewich, B.J., Tackett, J.L., Kar, J., Garnier, A., Vaughan, M.A., Hunt, B., 2016. CALIOP calibration: version 4.0 algorithm updates. EPJ Web of Conferences 119, 04013. https://doi.org/10.1051/epjconf/201611904013.
Giles, D., Slutsker, I., Schafer, J., Sorokin, M.G., Smirnov, A., Eck, T.F., et al., 2019. Uncertainty and Bias in AERONET nighttime AOD measurements. AGUFM 2019, A23R–3050.
Hsu, N.C., Lee, J., Sayer, A.M., Kim, W., Bettenhausen, C., Tsay, S.-C., 2019. VIIRS deep blue aerosol products over land: extending the EOS long-term aerosol data records.

J. Geophys. Res. Atmos. 124 (7), 4026–4053. https://doi.org/10.1029/2018JD029688.
Jiang, Xiaodong, et al., 2024. Characteristics of daytime-and-nighttime AOD differences over China: A perspective from CALIOP satellite observations and GEOS-Chem model simulations. J. Geophys. Res.: Atmos. 129 (8), e2023JD039158.
Johnson, R.S., Zhang, J., Hyer, E.J., Miller, S.D., Reid, J.S., 2013. Preliminary investigations toward nighttime aerosol optical depth retrievals from the VIIRS day/night band. Atmos. Meas. Tech. 6 (5), 1245–1255. https://www.atmos-meas-tech.net/6/1245/2013/.
Kahn, R.A., Nelson, D.L., Garay, M.J., Levy, R.C., Bull, M.A., Diner, D.J., et al., 2009. MISR aerosol product attributes and statistical comparisons with MODIS. IEEE Trans. Geosci. Remote Sens. 47 (12), 4095–4114.
Klüser, L., Martynenko, D., Holzer-Popp, T., 2011. Thermal infrared remote sensing of mineral dust over land and ocean: a spectral SVD based retrieval approach for IASI. Atmospheric Measurement Techniques Discussions 4 (1), 461–509.
Lanzaco, B.L., Olcese, L.E., Palancar, G.G., Toselli, B.M., 2017. An Improved Aerosol Optical Depth Map Based on Machine-Learning and MODIS Data: Development and Application in South America.
Lary, D.J., Remer, L., MacNeill, D., Roscoe, B., Paradise, S., 2009. Machine learning and bias correction of MODIS aerosol optical depth. IEEE Geosci. Remote Sens. Lett. 6 (4), 694–698.
Lee, S.-S., Lee, E.-H., Sohn, B.-J., Lee, H.C., Cho, J.H., Ryoo, S.-B., 2017. Improved dust forecast by assimilating MODIS IR-based nighttime AOT in the ADAM2 model. SOLA 13, 192–198.
Levy, R., Mattoo, S., Munchak, L., Remer, L., Sayer, A., Patadia, F., Hsu, N., 2013. The collection 6 MODIS aerosol products over land and ocean. Atmos. Meas. Tech. 6 (11), 2989.
Li, X., Ma, R., Zhang, Q., Li, D., Liu, S., He, T., Zhao, L., 2019. Anisotropic characteristic of artificial light at night–systematic investigation with VIIRS DNB multi-temporal observations. Remote Sens. Environ. 233, 111357.
Lu, Z., Wang, J., Chen, X., Zeng, J., Wang, Y., Xu, X., et al., 2023. First mapping of monthly and diurnal climatology of Saharan dust layer height over the Atlantic Ocean from EPIC/DSCOVR in deep space. Geophys. Res. Lett. 50 (5) e2022GL102552.
Lyapustin, A., Wang, Y., Laszlo, I., Kahn, R., Korkin, S., Remer, L., et al., 2011. Multiangle implementation of atmospheric correction (MAIAC): 2. Aerosol algorithm. Journal of Geophysical Research: Atmospheres 116 (D3). https://doi.org/10.1029/2010JD014986.
Martins, V.S., Lyapustin, A., de Carvalho, L.A., Barbosa, C.C.F., Novo, E.M.L., d. M., 2017. Validation of high-resolution MAIAC aerosol product over South America. J. Geophys. Res. Atmos. 122 (14), 7537–7559.
McGill, M.J., Yorks, J.E., Scott, V.S., Kupchock, A.W., Selmer, P.A., 2015. The Cloud-Aerosol Transport System (CATS): A Technology Demonstration on the International Space Station (Paper presented at the Lidar remote sensing for environmental monitoring XV).
McHardy, T.M., Zhang, J., Reid, J.S., Miller, S.D., Hyer, E.J., Kuehn, R.E., 2015. An improved method for retrieving nighttime aerosol optical thickness from the VIIRS day/night band. Atmos. Meas. Tech. 8 (11), 4773–4783. https://www.atmos-meas-tech.net/8/4773/2015/.
Miller, S.D., Turner, R.E., 2009. A dynamic lunar spectral irradiance data set for NPOESS/VIIRS day/night band nighttime environmental applications. IEEE Trans. Geosci. Remote Sens. 47 (7), 2316–2329.
Miller, S.D., Straka, W., Mills, S.P., Elvidge, C.D., Lee, T.F., Solbrig, J., et al., 2013. Illuminating the capabilities of the Suomi National Polar-Orbiting Partnership (NPP) visible infrared imaging radiometer suite (VIIRS) day/night band. Remote Sens. (Basel) 5 (12), 6717–6766. https://www.mdpi.com/2072-4292/5/12/6717.
Min, M., Zheng, J., Zhang, P., Hu, X., Chen, L., Li, X., et al., 2020. A low-light radiative transfer model for satellite observations of moonlight and earth surface light at night. Journal of Quantitative Spectroscopy and Radiative Transfer 247, 106954.
Min, M., Zhang, L., Zhang, P., Yao, Z., 2021. Can the earth–moon distance influence the accuracy of lunar irradiance with the plane-parallel assumption in atmospheric radiative transfer at night? J. Atmos. Sci. 78 (8), 2459–2469.
Niang, A., Badran, F., Moulin, C., Crépon, M., Thiria, S., 2006. Retrieval of aerosol type and optical thickness over the Mediterranean from SeaWiFS images using an automatic neural classification method. Remote Sens. Environ. 100 (1), 82–94.
Oppenheim, A.V., Willsky, A.S., Nawab, S.H., Ding, J.-J., 1997. Signals and Systems, Vol. 2. Prentice hall Upper, Saddle River, NJ.
Peyridieu, S., Chédin, A., Capelle, V., Tsamalis, C., Pierangelo, C., Armante, R., et al., 2013. Characterisation of dust aerosols in the infrared from IASI and comparison with PARASOL, MODIS, MISR, CALIOP, and AERONET observations. Atmos. Chem. Phys. 13 (12), 6065–6082. https://acp.copernicus.org/articles/13/6065/2013/.
Pierangelo, C., Chédin, A., Heilliette, S., Jacquinet-Husson, N., Armante, R., 2004. Dust altitude and infrared optical depth from AIRS. Atmos. Chem. Phys. 4 (7), 1813–1822. https://acp.copernicus.org/articles/4/1813/2004/.
Polivka, T.N., Wang, J., Ellison, L.T., Hyer, E.J., Ichoku, C.M., 2016. Improving Nocturnal Fire Detection With the VIIRS Day–Night Band. IEEE Trans. Geosci. Remote Sens. 54 (9), 5503–5519.
Pörtner, H.-O., Roberts, D.C., Adams, H., Adler, C., Aldunce, P., Ali, E., et al., 2022. Climate Change 2022: Impacts, Adaptation and Vulnerability. IPCC Sixth Assessment Report.
Pye, H.O.T., Ward-Caviness, C.K., Murphy, B.N., Appel, K.W., Seltzer, K.M., 2021. Secondary organic aerosol association with cardiorespiratory disease mortality in the United States. Nat. Commun. 12 (1), 7215. https://doi.org/10.1038/s41467-021-27484-1.
Randles, C., Da Silva, A., Buchard, V., Colarco, P., Darmenov, A., Govindaraju, R., et al., 2017. The MERRA-2 aerosol reanalysis, 1980 onward. Part I: system description and data assimilation evaluation. J. Climate 30 (17), 6823–6850.
Remer, L.A., Kaufman, Y., Tanré, D., Mattoo, S., Chu, D., Martins, J.V., et al., 2005. The MODIS aerosol algorithm, products, and validation. J. Atmos. Sci. 62 (4), 947–973.
Richon, C., Dutay, J.-C., Dulac, F., Wang, R., Balkanski, Y., Nabat, P., et al., 2018. Modeling the impacts of atmospheric deposition of nitrogen and desert dust-derived phosphorus on nutrients and biological budgets of the Mediterranean Sea. Prog. Oceanogr. 163, 21–39. https://www.sciencedirect.com/science/article/pii/S0079661116301811.
Rizzolo, J.A., Barbosa, C.G.G., Borillo, G.C., Godoi, A.F.L., Souza, R.A.F., Andreoli, R.V., et al., 2017. Soluble iron nutrients in Saharan dust over the Central Amazon rainforest. Atmos. Chem. Phys. 17 (4), 2673–2687. https://acp.copernicus.org/articles/17/2673/2017/.
Sawyer, V., Levy, R.C., Mattoo, S., Cureton, G., Shi, Y., Remer, L.A., 2020. Continuing the MODIS dark target aerosol time series with VIIRS. Remote Sens. (Basel) 12 (2), 308.
Sayer, A., Hsu, N., Lee, J., Bettenhausen, C., Kim, W., Smirnov, A., 2018. Satellite Ocean aerosol retrieval (SOAR) algorithm extension to S-NPP VIIRS as part of the "deep blue" aerosol project. J. Geophys. Res. Atmos. 123 (1), 380–400.
Schlyter, P., 2010. Computing planetary positions-a tutorial with worked examples. Downloaded March, 26,. 2010.
Schueler, C.F., Clement, J.E., Ardanuy, P.E., Welsch, C., DeLuccia, F., Swenson, H., 2002. NPOESS VIIRS sensor design overview (Paper presented at the Earth Observing Systems VI).
Singh, A., Aung, T., 2005. Effect of barometric pressure on sea level variations in the Pacific region. The South Pacific Journal of Natural and Applied Sciences 23 (1), 9–15.
Singh, J., Noh, Y.-J., Agrawal, S., Tyagi, B., 2019. Dust detection and aerosol properties over arabian sea using MODIS data. Earth Syst. Environ. 3 (1), 139–152.
Sokolik, I.N., 2002. The spectral radiative signature of wind-blown mineral dust: Implications for remote sensing in the thermal IR region. Geophysical Research Letters 29 (24), 7-1.
Song, J., Wang, J., Xia, X., Lin, R., Wang, Y., Zhou, M., Fu, D., 2021. Characterization of urban Heat Islands using City lights: insights from MODIS and VIIRS DNB observations. Remote Sens. (Basel) 13 (16), 3180. https://www.mdpi.com/2072-4292/13/16/3180.
Sun, K., Su, Q., Ming, Y., 2019. Dust storm remote sensing monitoring supported by MODIS land surface reflectance database. Remote Sensing 11 (15), 1772.
Tackett, J.L., Winker, D.M., Getzewich, B.J., Vaughan, M.A., Young, S.A., Kar, J., 2018. CALIPSO lidar level 3 aerosol profile product: version 3 algorithm design. Atmos. Meas. Tech. Discuss. 2018, 1–39. https://www.atmos-meas-tech-discuss.net/amt-2018-97/.
Tao, M., Chen, J., Xu, X., Man, W., Xu, L., Wang, L., et al., 2023. A robust and flexible satellite aerosol retrieval algorithm for multi-angle polarimetric measurements with physics-informed deep learning method. Remote Sens. Environ. 297, 113763.
Tilstra, L., Tuinder, O., Wang, P., Stammes, P., 2017. Surface reflectivity climatologies from UV to NIR determined from earth observations by GOME-2 and SCIAMACHY. J. Geophys. Res. Atmos. 122 (7), 4084–4111.
Vandenbussche, S., Kochenova, S., Vandaele, A.C., Kumps, N., De Mazière, M., 2013. Retrieval of desert dust aerosol vertical profiles from IASI measurements in the TIR atmospheric window. Atmos. Meas. Tech. 6 (10), 2577–2591. https://amt.copernicus.org/articles/6/2577/2013/.
Walther, A., Heidinger, A.K., Miller, S., 2013. The expected performance of cloud optical and microphysical properties derived from Suomi NPP VIIRS day/night band lunar reflectance. J. Geophys. Res. Atmos. 118 (23), 13,230-213,240.
Wang, J., Christopher, S.A., Reid, J.S., Maring, H., Savoie, D., Holben, B.N., et al., 2003. GOES 8 retrieval of dust aerosol optical thickness over the Atlantic Ocean during PRIDE. J. Geophys. Res. Atmos. 108 (D19) https://doi.org/10.1029/2002JD002494.
Wang, J., Nair, U.S., Christopher, S.A., 2004. GOES 8 aerosol optical thickness assimilation in a mesoscale model: online integration of aerosol radiative effects. J. Geophys. Res. Atmos. 109 (D23) https://doi.org/10.1029/2004JD004827.
Wang, J., Xu, X., Ding, S., Zeng, J., Spurr, R., Liu, X., et al., 2014. A numerical testbed for remote sensing of aerosols, and its demonstration for evaluating retrieval synergy from a geostationary satellite constellation of GEO-CAPE and GOES-R. J. Quant. Spectrosc. Radiat. Transf. 146, 510–528. http://www.sciencedirect.com/science/article/pii/S0022407314001368.
Wang, J., Aegerter, C., Xu, X., Szykman, J.J., 2016. Potential application of VIIRS day/night band for monitoring nighttime surface PM2.5 air quality from space. Atmos. Environ. 124, 55–63. http://www.sciencedirect.com/science/article/pii/S1352231015305215.
Wang, J., Roudini, S., Hyer, E.J., Xu, X., Zhou, M., Garcia, L.C., et al., 2020a. Detecting nighttime fire combustion phase by hybrid application of visible and infrared radiation from Suomi NPP VIIRS. Remote Sens. Environ. 237, 111466. http://www.sciencedirect.com/science/article/pii/S0034425719304857.
Wang, Y., Wang, J., Zhou, M., Henze, D.K., Ge, C., Wang, W., 2020b. Inverse modeling of SO 2 and NO x emissions over China using multisensor satellite data–part 2: downscaling techniques for air quality analysis and forecasts. Atmospheric Chemistry and Physics 20 (11), 6651–6670.
Wang, J., Zhou, M., Xu, X., Roudini, S., Sander, S.P., Pongetti, T.J., et al., 2020c. Development of a nighttime shortwave radiative transfer model for remote sensing of nocturnal aerosols and fires from VIIRS. Remote Sens. Environ. 241, 111727. http://www.sciencedirect.com/science/article/pii/S0034425720300973.
Wang, Y., Wang, J., Levy, R.C., Shi, Y.R., Mattoo, S., Reid, J.S., 2021. First retrieval of AOD at fine resolution over shallow and turbid coastal waters from MODIS. Geophys. Res. Lett. 48 (17) https://doi.org/10.1029/2021GL094344 e2021GL094344.

Westberry, T., Behrenfeld, M., Shi, Y., Yu, H., Remer, L., Bian, H., 2023. Atmospheric nourishment of global ocean ecosystems. Science 380 (6644), 515–519.
Winker, D.M., Hunt, W.H., 2007. Initial performance assessment of CALIOP. Geophys. Res. Lett. 34 (19).
Winker, D.M., Vaughan, M.A., Omar, A., Hu, Y., Powell, K.A., Liu, Z., et al., 2009. Overview of the CALIPSO Mission and CALIOP data processing algorithms. J. Atmos. Oceanic Tech. 26 (11), 2310–2323. https://doi.org/10.1175/2009JTECHA1281.1.
Xiao, Q., Zhou, M., Lyu, Y., Lu, J., Zhang, K., Figueiro, M., et al., 2023a. County-Level Artificial Light at Night (ALAN) in the Contiguous US (2012–2019): Spatial Variations (Temporal Trends and Environmental Justice Analyses).
Xiao, Q., Zhou, M., Lyu, Y., Lu, J., Zhang, K., Figueiro, M., et al., 2023b. County-Level Artificial Light at Night (ALAN) in the Contiguous US (2012–2019): Spatial Variations (Temporal Trends and Environmental Justice Analyses).
Xu, X., Wang, J., 2015. Retrieval of aerosol microphysical properties from AERONET photopolarimetric measurements: 1. Information content analysis. J. Geophys. Res. Atmos. 120 (14), 7059–7078. https://doi.org/10.1002/2015JD023108.
Xu, X., Wang, J., Wang, Y., Zeng, J., Torres, O., Yang, Y., et al., 2017. Passive remote sensing of altitude and optical depth of dust plumes using the oxygen a and B bands: first results from EPIC/DSCOVR at Lagrange-1 point. Geophys. Res. Lett. 44 (14), 7544–7554. https://doi.org/10.1002/2017GL073939.
Yu, H., Tan, Q., Zhou, L., Zhou, Y., Bian, H., Chin, M., et al., 2021. Observation and modeling of the historic "Godzilla" African dust intrusion into the Caribbean Basin and the southern US in June 2020. Atmos. Chem. Phys. 21 (16), 12359–12383. https://acp.copernicus.org/articles/21/12359/2021/.
Yuan, Q., Shen, H., Li, T., Li, Z., Li, S., Jiang, Y., et al., 2020. Deep learning in environmental remote sensing: achievements and challenges. Remote Sens. Environ. 241, 111716.
Zheng, J., Zhang, Z., Garnier, A., Yu, H., Song, Q., Wang, C., et al., 2022. The thermal infrared optical depth of mineral dust retrieved from integrated CALIOP and IIR observations. Remote Sens. Environ. 270, 112841.
Zheng, J., Zhang, Z., Yu, H., Garnier, A., Song, Q., Wang, C., et al., 2023. Thermal infrared dust optical depth and coarse-mode effective diameter over oceans retrieved from collocated MODIS and CALIOP observations. Atmospheric Chemistry and Physics 23 (14), 8271–8304.
Zhou, M., Wang, J., Chen, X., Xu, X., Colarco, P.R., Miller, S.D., et al., 2021. Nighttime smoke aerosol optical depth over U.S. rural areas: first retrieval from VIIRS moonlight observations. Remote Sens. Environ. 267, 112717. https://www.sciencedirect.com/science/article/pii/S0034425721004375.
Zhou, M., Wang, J., Garcia, L.C., Chen, X., da Silva, A.M., Wang, Z., et al., 2023. Enhancement of nighttime fire detection and combustion efficiency characterization using Suomi-NPP and NOAA-20 VIIRS instruments. IEEE Trans. Geosci. Remote Sens. 61, 1–20.